The Planetary Science Journal, 6:38 (27pp), 2025 February https://doi.org/10.3847/PSJ/ad944d
© 2025. The Author(s). Published by the American Astronomical Society.
OPEN ACCESS

Dimorphos's Material Properties and Estimates of Crater Size from the DART Impact

Angela M. Stickle[1], Kathryn M. Kumamoto[2], Dawn M. Graninger[1], Mallory E. DeCoster[1], Wendy K. Caldwell[3], Jason M. Pearl[2], J. Michael Owen[2], Olivier Barnouin[1], Gareth S. Collins[4], R. Terik Daly[1], Isabel Herreros[5], Jens Ormö[5], Jessica Sunshine[6], Carolyn M. Ernst[1], Toshi Hirabayashi[7], Simone Marchi[8], Laura Parro[9], Harrison Agrusa[6,10], Megan Bruck Syal[2], Nancy L. Chabot[2], Andy F. Cheng[1], Thomas M. Davison[4], Elisabetta Dotto[11], Eugene G. Fahenstock[12], Fabio Ferrari[13], Martin Jutzi[14], Alice Lucchetti[15], Robert Luther[16], Nilanjan Mitra[17], Maurizio Pajola[15], Sabina Raducan[14], KT Ramesh[17], Andrew S. Rivkin[1], Alessandro Rossi[18], Paul Sánchez[19], Stephen R. Schwartz[20], Stefania Soldini[21], Jordan K. Steckloff[20], Filippo Tusberti[15], Kai Wünnemann[16], and Yun Zhang[6]
[1] Johns Hopkins Applied Physics Laboratory, 11100 Johns Hopkins Road, Laurel, MD, 20723, USA; angela.stickle@jhuapl.edu
[2] Lawrence Livermore National Laboratory, Livermore, CA, USA
[3] Los Alamos National Laboratory, Los Alamos, NM, USA
[4] Department of Earth Science & Engineering, Imperial College, London, UK
[5] Centro de Astrobiología (CAB) CSIC-INTA, Carretera de Ajalvir km4, 28850 Torrejón de Ardoz, Spain
[6] University of Maryland, College Park, MD, USA
[7] Daniel Guggenheim School of Aerospace Engineering, Georgia Institute of Technology, Atlanta, GA 30332, USA
[8] Southwest Research Institute, Boulder, CO, USA
[9] Universidad de Alicante, Spain
[10] Universite Côte d'Azur, Observatoire de la Côte d'Azur, Centre National de la Recherche Scientifique, Laboratoire Lagrange, Nice, France
[11] INAF-Osservatorio Astronomico di Roma, Rome, Italy
[12] Jet Propulsion Laboratory, California Institute of Technology, Pasadena, CA, USA
[13] Department of Aerospace Science and Technology, Politecnico di Milano, Milan 20159, Italy
[14] Space Research and Planetary Sciences, Physikalisches Institut, University of Bern, Bern, Switzerland
[15] INAF Osservatorio Astronomico di Padova, Padua, Italy
[16] Museum für Naturkunde, Leibniz-Institut für Evolutions- und Biodiversitätsforschung, Berlin, Germany
[17] Department of Mechanical Engineering, Johns Hopkins University, Baltimore MD, USA
[18] Istituto di Fisica Applicata "Nello Carrara" (IFAC-CNR), Sesto Fiorentino 50019, Italy
[19] University of Colorado, Boulder, CO, USA
[20] Planetary Science Institute, Tucson, AZ, USA
[21] Department of Mechanical & Aerospace Engineering, University of Liverpool, Liverpool L69 3GH, UK
Received 2024 July 29; revised 2024 November 12; accepted 2024 November 13; published 2025 February 4

Abstract

On 2022 September 26, the Double Asteroid Redirection Test (DART) spacecraft intentionally collided with Dimorphos, the moon of the binary asteroid system 65803 Didymos. This collision provided the first full-scale test of a kinetic impactor for planetary defense. Images from DART's DRACO camera revealed Dimorphos to be an oblate spheroid covered in boulders of varying sizes and shapes. Very little was known about Dimorphos prior to DART's impact, including its shape, structure, and material properties. Approach observations and those following the DART impact have provided crucial knowledge that narrows the parameter space relevant to modeling the impact into Dimorphos. Here we present the results of a suite of hydrocode simulations of the DART impact on Dimorphos. Despite remaining uncertainties, initial models of DART's kinetic impact provide important information about the results of DART (e.g., potential crater size and morphology, ejecta mass) and the properties of Dimorphos. Simulations here suggest that Dimorphos has near-surface strength ranging from a few Pascals to tens of kPa, which corresponds to crater sizes of ∼40–60 m. Simulated crater sizes provide a crucial comparison metric for the European Space Agency Hera mission when it arrives at the Didymos system. Hera's measurement of crater size in combination with measurement of Dimorphos's mass will allow us to assess our simulations and provide the information needed to make the DART impact experiment both the first test of a planetary defense mitigation mission and the first full-scale planetary defense simulation validation exercise.

Unified Astronomy Thesaurus concepts: Asteroids (72); Craters (2282); Impact phenomena (779); Planetary science (1255)

Materials only available in the online version of record: animation, data behind figure

1. Introduction

The Double Asteroid Redirection Test (DART; A. F. Cheng et al. 2018; A. S. Rivkin et al. 2021) is NASA's first planetary defense demonstration of asteroid deflection using a kinetic impactor. The DART spacecraft impacted Dimorphos, the secondary of the (65803) Didymos system, on 2022 September 26 at 23:14:24.183 ± 0.004 UTC (R. T. Daly et al. 2023). The DART collision shortened the orbital period of Dimorphos around Didymos by 33 minutes (C. A. Thomas et al. 2023), which corresponds to an orbital velocity change, ΔV, of –2.7 mm s^{-1}, and a momentum enhancement from the ejecta, β, of 2.2–4.9, depending on the poorly constrained density of Dimorphos (A. F. Cheng et al. 2023).

Original content from this work may be used under the terms of the Creative Commons Attribution 4.0 licence. Any further distribution of this work must maintain attribution to the author(s) and the title of the work, journal citation and DOI.

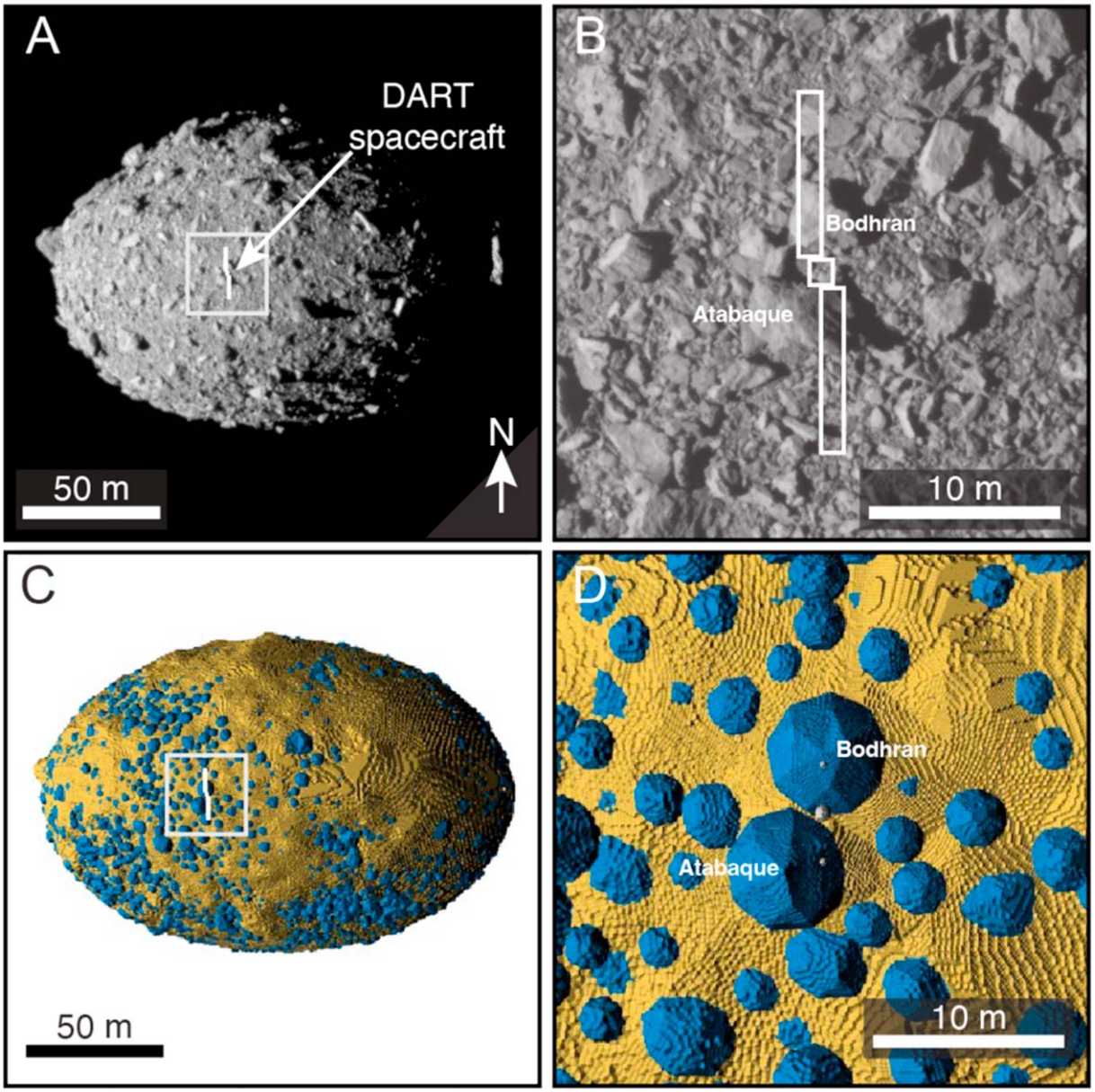

Figure 1. Initial observations of Dimorphos from DART, showing (a) a portion of the final full-frame image of Dimorphos, 11 s before DART's impact at 68 km distance (DRACO image dart_0401930039_14119_01_iof.fits), and (b) a closeup of the impact site 2 s before DART's impact at 12 km distance (DRACO image and dart_0401930049_43695_01_iof.fits) with an outline of the DART spacecraft overlain for context. (c) Simulated rubble-pile target designed to match panel (a). (d) Closeup of a simulated impact site showing the simplified DART spacecraft used in simulations (three aluminum spheres). The impact velocity vector is into the page.

Approach images from DART's DRACO camera (Z. J. Fletcher et al. 2018) revealed Dimorphos to be a rubble-covered oblate spheroid (R. T. Daly et al. 2023). Follow-on images from the ASI-led cubesat LICIACube (E. Dotto et al. 2021) and Earth- and space-based telescopes revealed spectacular ejecta rays immediately following impact, with a complicated ejecta structure and ejected boulders (T. L. Farnham et al. 2023; D. Jewitt et al. 2023; T. Kareta et al. 2023; J. Y. Li et al. 2023; E. Dotto et al. 2024; Figure 1). Ejecta speeds during the early evolution phase were found to range from a few tens of meters per second up to roughly 500 m s^{-1} (E. Dotto et al. 2024). LICIACube images also revealed that the geometry of the ejecta plume is a nonaxisymmetric cone, with the opening angle ranging from approximately 102° to 138° (M. Hirabayashi et al. 2024; J. D. P. Deshapriya et al. 2023). Further analyses of ground-based observations provide estimates for the amount of ejecta generated, (1–6) $\times 10^7$ kg (A. Graykowski et al. 2023; Y. Kim & D. Jewitt 2023; F. C. Moreno et al. 2023; F. Ferrari et al. 2024; D. C. Richardson et al. 2024; N. X. Roth et al. 2023).

A key objective of the DART mission was to quantify the contribution of impact ejecta to the change in the momentum of Dimorphos after impact. The relative momentum change imparted to the asteroid by a kinetic impactor is composed of two parts: the incident momentum of the impactor (here the DART spacecraft), and the momentum of the impact ejecta that escapes Dimorphos, providing a thrust in the opposite direction of the ejecta velocity. The momentum enhancement factor, β, is the ratio of the net change in momentum to the incident impactor momentum and quantifies the relative contribution of

ejecta. Equation (1) shows its simplest form:

$$\beta = \frac{p_A \cdot \hat{x}}{p_{sc} \cdot \hat{x}} = \frac{(p_{sc} - p_e) \cdot \hat{x}}{p_{sc} \cdot \hat{x}}, \quad (1)$$

where p is momentum, $\hat{x}$ is a unit vector in the direction of interest, and subscripts A, e, and sc refer to the asteroid, ejecta, and spacecraft, respectively. The ejecta momentum is often roughly in the opposite direction of the incident spacecraft momentum, meaning that any ejecta production will enhance the net momentum change. In a perfectly inelastic collision, no ejecta are generated and β is unity. A high efficiency $\beta > 2$ indicates that the ejecta momentum makes a larger contribution to the momentum change of the asteroid than the incident spacecraft momentum.

Using constraints provided by direct observations of the Didymos system and resulting ejecta, a set of impact simulations can be used to place bounds on crater size and Dimorphos's material properties. Here we present impact simulations that use key DART observables—the orbital velocity and period change, ejecta characteristics and estimated total ejecta mass, and surface morphology and shape of Dimorphos—to reduce the uncertainty in Dimorphos's material properties and predict the size of the crater left by the DART impact. We will discuss how the observations following the DART impact (e.g., period change, ejecta, surface morphology), combined with the insights gained from impact simulations, help reduce the uncertainty in Dimorphos's material properties and provide estimates of crater size. Synthesizing results from a variety of simulations provides one of the best ways to evaluate potential "best-fit" properties of Dimorphos. The constraints from these simulations provide additional information regarding how data from Hera can further constrain Dimorphos's material properties after it arrives at the Didymos system.

2. Analysis of Pre-impact Simulations

The DART impact was preceded by a decade-long effort to benchmark numerical impact models, understand how to effectively model the outcome of the DART impact, and determine how to constrain asteroid properties from numerical models (M. Bruck Syal et al. 2016; A. M. Stickle et al. 2015, 2017, 2020, 2022; K. M. Kumamoto et al. 2022; R. Luther et al. 2022; J. M. Owen et al. 2022; S. D. Raducan et al. 2019, 2022a, 2022b; S. D. Raducan & M. Jutzi 2022). Little was known about Dimorphos prior to DART's arrival, and this limited information posed challenges for predicting the outcome of the impact, as key asteroid properties were unknown. A synthesis of nearly 10 yr of pre-impact simulations covering a very wide set of possible material properties predicted that ejecta would enhance the momentum change by a factor of β between 1 and 5, depending on the material properties of Dimorphos (A. M. Stickle et al. 2022).

Material behavior can be described in many ways, and usually in impact hydrocodes material models include information about, for example, the material porosity, coefficient of internal friction, elastic properties (e.g., Young's modulus, bulk modulus, Poisson's ratio), and a variety of strength terms. Many specific deformation mechanisms (e.g., representations of shearing behavior, compression, bulking, fracture/fragmentation) can be considered and are represented in different codes in different ways. Regardless of the implementation, some specific relationships between material behavior and resultant momentum enhancement were identified prior to the DART impact (e.g., A. M. Stickle et al. 2022). In general, pre-impact simulations suggested that β is strongly affected by target cohesion (taken here to be the yield strength of damaged material at zero pressure), the coefficient of internal friction, and the target porosity (J. D. Walker & S. Chocron 2011; A. M. Stickle et al. 2015, 2017, 2022; M. Bruck Syal et al. 2016; S. D. Raducan et al. 2019; E. S. G. Rainey et al. 2020; K. M. Kumamoto et al. 2022; R. Luther et al. 2022; S. D. Raducan & M. Jutzi 2022). Other parameters, such as target shape and internal structure, can affect β, but the effects are subtler and depend on the specifics of the shape combined with impact angle and the near-surface structure.

The shear strength models employed in impact hydrocodes typically define an intact and a damaged strength envelope. The former describes the pressure-dependent shear strength in the pristine, unfractured material, whereas the latter describes the residual pressure-dependent shear strength after complete fragmentation of the material. The parameters that describe target porosity and this residual shear strength typically exert the most influence on deflection efficiency and crater size (A. M. Stickle et al. 2022).

A. M. Stickle et al. (2022) documented predictions of β from 225 simulations of the DART impact by several different numerical impact codes using many different possible target material property combinations. Comparing these numerical predictions of β with the observed outcome provides some preliminary constraints on the material properties of Dimorphos. For these simulations, we measure the mismatch between the simulated β_{sim} and the observed β-value given by A. F. Cheng et al. (2023) as

$$\zeta = (\beta_{sim} - \beta_{obs})/\beta_{obs}. \quad (2)$$

We then examine ζ as a function of individual material properties. For this setup, we compare simulation results to the value of β determined for the average density estimate of $2400\ \mathrm{kg\ m^{-3}} \pm 300\ \mathrm{kg\ m^{-3}}$ (1σ; A. F. Cheng et al. 2023):

$$\beta = (3.61 \pm 0.2)\frac{\rho}{2400\ \mathrm{kg\ m^{-3}}} - 0.03 \pm 0.02. \quad (3)$$

While no clear dependence of ζ on either friction coefficient or target porosity is apparent in this complex data set, there is a clear negative correlation between ζ and the cohesion (the yield strength of damaged target material at zero pressure, Y_d). Significant scatter around this trend demonstrates the contribution of other properties, including porosity, density, material choice, and more. In general, however, simulations that predict a value for β consistent with the central DART outcome of $3.61^{+0.19}_{-0.25}$ (1σ; A. F. Cheng et al. 2023) to within 2σ uncertainty mostly employed a target cohesion of $\leqslant 1$ kPa (Figure 2), though we do not take into account any variation of β with density. Simulations with a cohesion >1 kPa tend to predict a lower β than observed, and simulations with a cohesion <1 kPa tend to predict a higher β than observed. This suggests that an upper bound on the effective cohesion of a homogenous, monolithic Dimorphos is within the kPa regime.

Most of the simulations documented in A. M. Stickle et al. (2022) assumed a homogeneous target with uniform material properties. The observed rubble-pile surface suggests that the effect of large near-surface boulders, many with diameters larger than the spacecraft bus, may play an important role in

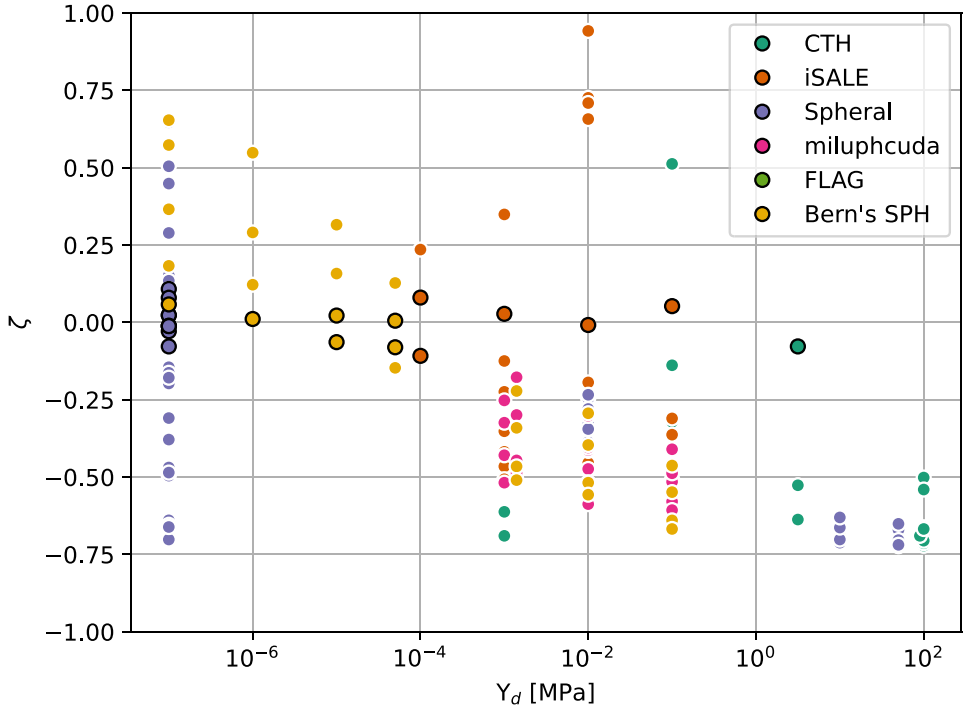

Figure 2. Mismatch between simulated and observed β for the DART impact as a function of target cohesion for pre-launch DART impact simulations documented in A. M. Stickle et al. (2022). Colors represent different codes used in simulations. Points circled in black indicate simulations that fall within a 2σ uncertainty of the DART β of 3.61. Simulations with a Y_d of 0 Pa are plotted at 0.1 Pa.

modulating momentum transfer, either by armoring the surface (E. Tatsumi & S. Sugita 2018; M. E. DeCoster et al. 2024) and reducing the effective β or enhancing the impact coupling efficiency (O. S. Barnouin et al. 2019) and increasing the effective β. If boulders armor the surface, this could imply that the effective cohesion of the matrix between boulders is considerably less than 1 kPa. Conversely, if the boulders enhance the impact coupling efficiency, the effective cohesion of the matrix between the boulders would be considerably more than 1 kPa.

Information gathered from pre-impact work, as well as DART observations of the Didymos system, provides intuition for likely material properties of Dimorphos. The rubble-covered surface (Figure 1), abundant ejecta, and magnitude of the period change (C. A. Thomas et al. 2023) rule out bulk strength properties similar to low-porosity, monolithic competent rock (e.g., strength of hundreds of MPa) for Dimorphos, which would have resulted in a deflection that is too small and a resulting β that is too low. However, images suggest that Dimorphos could possess well-connected aggregates with plausibly significant strength below the surface (perhaps composed of slightly damaged and weakened ordinary chondrites; S. Marchi et al. 2015; S. L. Murchie et al. 2015), indicating that (near) strengthless material (cohesion $<$1 Pa) throughout the asteroid is unlikely.

3. Methods

3.1. Simulation Setup

In all simulations, we model Dimorphos as a composite of two discrete materials, boulders and matrix. The boulder material is used to model boulders that are large enough to be explicitly resolved (here diameter $>$2 m). The matrix material is used to model the bulk response of the cobbles, pebbles, and dust that are too small to be resolved explicitly. The setup of this asteroid structure, and how it is implemented in three different shock physics codes, is described in the remainder of Section 3, but first we must take a detour to discuss nomenclature related to the term "strength."

In this study, we refer to several different types of strength, each of which defines a different type of transition in the material's behavior. The three forms of strength we are concerned with are the yield strength, which defines the onset of plastic flow; the crush strength, which defines a material's resistance to porous compaction; and the fracture strength, which controls the transition from competent rock to damaged rubble. In our simulations, these "strengths" are not necessarily single valued, but rather vary as a function of the state (e.g., pressure, temperature). When this is the case, we use parameters from these functions to characterize materials as "strong" or "weak." In our discussion of yield strength, we will refer to two model parameters, the yield strength at zero pressure and the friction coefficient (i.e., the linear coefficient with respect to pressure). For brevity, we truncate "yield strength at zero pressure" to "yield strength," and we use the term "cohesion" to mean the "yield strength at zero pressure of fully damaged material." "Cohesive strength" is synonymous with "cohesion." The nomenclature related to the crush and fracture strength is somewhat more straightforward. We use "crush strength" to describe the pressure at which all pores have been compacted out of a material, and the fracture (or tensile) strength defines the threshold for the onset of damage. How exactly that threshold is defined varies somewhat between the different codes.

It is important to note that the functional forms employed in these strength models are mathematical approximations of observed behaviors and contextual to the application of hypervelocity impacts. They model the ensemble continuum

Table 1
Mechanical Parameters Describing the Asteroid Material

Variable	Label	Value	Notes
			Boulders
Porosity	ϕ_b	0.15	Value is intermediate between meteorites (>10%) from G. J. Flynn et al. (2018) and estimates for Bennu boulders (24%–38%) from B. Rozitis et al. (2022)
Intact yield strength	$Y_{i,b}$	1 MPa	Based on impact strength of boulders on Bennu of 0.44–1.7 MPa (R.-L. Ballouz et al. 2020)
Cohesive strength	$Y_{d,b}$	1 kPa[a]	Set to match $Y_{i,m}$
Poisson's ratio	ν_b	0.2	Measured from Chelyabinsk meteorite (S. A. Voropaev et al. 2017)
Coefficient of friction (intact)	$f_{i,b}$	1.0	Typical of terrestrial and lunar rocks (W. D. Carrier et al. 1991)
Coefficient of friction (damaged)	$f_{d,b}$	1.0	Set to $f_{i,b}$
			Matrix
Porosity	ϕ_m	VARIABLE	Three matrix porosities are explored in this study (0.223, 0.404, and 0.585) and are set to reach the bulk densities from R. T. Daly et al. (2023)
Intact yield strength	$Y_{i,m}$	1 kPa[a]	Estimate based on lunar regolith of 1–5 kPa (D. S. McKay et al. 1991)
Cohesive strength	$Y_{d,m}$	VARIABLE	Values of 10 Pa to 100 kPa are explored in this study.
Poisson's ratio	ν_m	0.25	Average for lunar regolith (W. D. Carrier et al. 1991)
Coefficient of friction (intact)	$f_{i,m}$	1.0	Average for lunar regolith (W. D. Carrier et al. 1991)
Coefficient of friction (damaged)	$f_{d,m}$	VARIABLE	

Notes. Parameters with single values were held constant across simulations.
Details on how these were implemented in each code can be found in the following sections.
[a] The cohesive strength of boulders and the yield strength of intact matrix material were increased to be equal to the cohesive strength of matrix material when $Y_{d,m} > 1$ kPa. In addition, the yield strength of intact matrix material was varied in a subset of simulations.

effects of complex subresolution physics. The parameters used in these models do not always directly correspond to specific values measured in the laboratory or in situ, particularly when those measurements are made outside the context of hypervelocity impacts. For example, in granular flows, a nonzero cohesion might serve as a simplified representation of hardening behavior due to granular interlocking. This manifests in the model as apparent cohesion, which is not the same thing as a higher *inherent* interparticle cohesion of the material, which tends to be due to electrostatic (P. Lee 1996), triboelectric (J. R. Marshall et al. 2005), solar radiation pressure (D. J. Scheeres 2005), and van der Waals forces (E. E. Asphaug 2009; D. D. J. Scheeres et al. 2010; N. Bahrani & P. K. Kaiser 2020; O. S. Barnouin et al. 2023).

3.1.1. General Simulation Parameters

The possible parameter space describing all of the relevant properties of an asteroid is exceedingly wide. In addition to the properties examined in previous studies for homogeneous targets compiled in A. M. Stickle et al. (2022), the clear presence of boulders on Dimorphos (Figure 1) means more than double the number of possible properties that could be varied, including the boulder material and the "matrix" material. However, prior work demonstrated that, at least for homogenous targets, four parameters have an outsized effect on the outcome of simulations of DART-like impacts (R. Luther et al. 2022; A. M. Stickle et al. 2022): the yield strength of damaged matrix material at zero pressure ($Y_{d,m}$, referred to in this study as cohesive strength), the coefficient of friction for damaged matrix material (f_d), the porosity of matrix material (ϕ_m), and the crush curve describing how porosity compacts under pressure. The numerical simulations reported primarily explore these four variables, and many properties are kept constant between simulations.

Many initial conditions are based on the actual DART experiment: the spacecraft mass, velocity, and orientation; the size and shape of Dimorphos; and details regarding the impact site (Figure 1) and local geology (Figure 1(d)). The spacecraft is modeled as a set of three spheres spaced 2.33 m apart, with a large central sphere containing 88% of the mass representing the spacecraft bus and two smaller spheres representing the spacecraft solar panel wings. J. M. Owen et al. (2022) suggest that we find that creating a simplified multiple impactor scenario (here using a "three-sphere" approximation) is fairly successful at reproducing the qualitative (and approximate quantitative) effects, and that was the approach taken as a best practice by the DART team. The outer shape of Dimorphos is modeled using the calculated Dimorphos shape model (g_00250mm_spc_obj_dimo_0000n00000_v003.obj) as the bounding surface for matrix material (R. T. Daly et al. 2023, T. Daly et al. 2023). While the shape model has since been updated (R. T. Daly et al. 2024), the geometry of the impact site remained relatively unchanged, as did the asteroid's volume. Thus, the updated shape model is expected to have only minor effects on these impact simulations. Finally, a single arrangement of boulders is used across all simulations, as described in the next section.

Across the majority of simulations, the following properties of the boulder material were held constant: porosity, intact and damaged coefficient of friction, and intact and damaged yield strength. In the matrix material, the intact yield strength and intact coefficients of friction were held constant. Reasonable values for these properties (Table 1) were assigned based on measurements from meteorites, lunar regolith, and returned asteroid material, or estimated based on in situ observations of asteroids. Exceptions to these constant values are listed in Appendix B (Tables B1–B6).

These simulations used the actual DART impact conditions and assumed a cohesive strength of matrix material between 10 Pa and 100 kPa to evaluate the potential upper limit for Dimorphos's strength. Several coefficients of friction for damaged matrix material were explored as well, varying between 0.6 and 1.0 based on measurements of lunar regolith

and granular materials (R. W. Krantz 1991; D. S. McKay et al. 1991). Matrix porosity was set to 36.7%, 27.7%, or 18.7%, which respectively correspond to a bulk density (ρ_b) value of 2.1, 2.4, or 2.7 g cm^{-3} (the estimated bulk density of Dimorphos with 1σ uncertainties; R. T. Daly et al. 2023).

3.1.2. The Simulated Rubble Pile

We used Spheral to generate a set of 27,117 boulders that were used to define the regions of Dimorphos modeled as boulder material in the three hydrocodes. These boulders represent 50% boulder fill in Dimorphos, and their size distribution matches the Weibull distribution that has been measured on Dimorphos's surface (M. Pajola et al. 2024). We explicitly assume that the size–frequency distribution at the surface of Dimorphos is representative of the interior of Dimorphos. The surface boulders visible in DRACO images with diameters between 1.0 and 16.0 m are well characterized by a Weibull distribution with the form

$$n = a \exp\left(-\left(\frac{x}{\lambda}\right)^k\right) \quad , \tag{4}$$

where n is the number of boulders per km^2, x is the boulder diameter, and a, k, and λ are fitting constants (Z. Fang et al. 1993). The best-fit parameters for the mentioned diameters are a = 9995083.23 boulders km^{-2}, $k = 0.39$, and λ = 0.033 m (M. M. Pajola et al. 2024).

In Spheral, we defined a minimum and maximum boulder diameter, the percentage of the asteroid to fill with boulders, and the size frequency distribution (SFD) of boulder sizes. We bound the smallest boulder diameter at 2 m and the largest boulder diameter at 20 m. Both our minimum and maximum boulder sizes are larger than the minimum and maximum boulder sizes observed on Dimorphos (1 and 16 m, respectively, for the distribution described above), but 20 m for the largest diameter is a reasonable rounding of the largest size observed on the surface, and the computational cost of decreasing the smallest diameter was significant. Any boulders smaller than 2 m are considered to be part of the matrix material filling in between the boulders.

Each boulder was created using the boulder SFD to determine a spherical diameter and then applying a random spherical harmonic perturbation (maximum order 4) to create a nonspherical boulder shape. Boulders were generated until the total volume of the best-fit ellipsoid of Dimorphos (R. T. Daly et al. 2023) filled by boulders was $\geqslant$50%. It is likely that the actual fill fraction of boulders within Dimorphos is >50%; however, this amount represents a limit due to computational resources. Then, starting with the largest boulder and working toward the smallest boulder, each boulder center was placed at a random unoccupied location inside of the asteroid ellipsoid and iteratively moved deeper within the surface until it either hits the maximum possible depth or encounters a preexisting boulder.

The boulder set was generated inside of the best-fit ellipsoid described in R. T. Daly et al. (2023) to simplify generation calculations, but the similarities between the ellipsoid and the shape model allow the boulder set to be easily translated between the two surface shapes. While this simplification creates some sections of asteroid without boulders directly on the surface (e.g., Figure 1), these regions are located away from the impact site, and there are many boulders directly below the surface. Thus, we do not expect these regions with a thin surface layer composed of matrix material to have an effect on our simulations. The morphology of the impact point and the boulder-strewn surface are informed by DRACO images (R. T. Daly et al. 2023): two roughly spherical, 3 m radius boulders are placed at the impact site representing the boulders Atabaque and Bodhran (Figure 1(d)), which were estimated to be ~6 m diameter boulders by R. T. Daly et al. (2023). The boulders generated by this technique were output and used in all simulations presented in this paper, regardless of the shock physics code used.

3.2. Hydrocodes Used in This Study

In this study, we used three different shock physics codes to simulate the DART impact into Dimorphos: CTH, Spheral, and FLAG. A brief description of the models used in each code is provided here, with additional details and parameters provided in Appendix B. We know that simulations, while a useful tool, do not always "simply" reflect reality. Despite our best efforts to align material parameters and models across codes, the material models used in our simulations are not standardized. Consequently, we anticipate that simulations performed with different codes will not yield identical results, even when attempting to closely match the input parameters. However, pre-impact comparisons show that when the same (or as similar as possible) material models are applied the difference between codes is not more than 15%–20% (A. M. Stickle et al. 2020, R. Luther et al. 2022), for the observables of interest here (e.g., momentum enhancement, crater size).

3.2.1. CTH

CTH is a multidimensional, multimaterial, large-deformation, strong shock wave hydrocode developed by Sandia National Laboratories (J. M. McGlaun et al. 1990; T. G. Trucano & J. M. McGlaun 1990) that is commonly used to model impacts of projectiles into asteroid-like surfaces (J. M. McGlaun et al. 1990; D. A. Crawford 1999; S. N. Quintana et al. 2015; A. M. Stickle et al. 2017) and has been used for a variety of planetary defense studies (A. M. Stickle et al. 2015, 2017, 2020, 2022; M. E. DeCoster et al. 2022).

The spatial resolution of the CTH grid is reported in terms of cells per projectile radius (cppr), which represents the resolution of the most highly refined regions of the mesh. We ran our simulations at a cppr = 1–5, corresponding to a spatial resolution of ~2–15 cm per cell. The ANEOS equation of state (EOS; S. L. Thompson & H. S. Lauson 1972; S. L. Thompson 1990) for Al-2024 and the Johnson–Cook strength model were used for the impactor (G. R. Johnson & W. H. Cook 1985). The ANEOS EOS was also used for the rubble-pile target with parameters (Table B3) appropriate for dunite (S. L. Thompson & H. S. Lauson 1972; S. L. Thompson 1990; R. M. Canup et al. 2013). Adaptive mesh refinement is used to improve computational efficiency by concentrating areas of high mesh refinement in areas of interest (D. A. Crawford 1999), allowing better tracking of shock waves and ejecta particles.

A pressure-dependent yield surface that incorporates thermal softening and density degradation (the "geo" material model) was used to model the matrix material, and the "BDL" material model (P. H. Schultz & D. A. Crawford 2016) was used for the boulders. The BDL model includes a pressure-dependent yield

and brittle damage model based on the popular strength/damage model described by G. S. Collins et al. (2004). BDL also incorporates a pressure-dependent melt curve to determine thermal softening (L. E. Senft & S. T. Stewart 2009) and a statistical crack spacing model (P. H. Schultz & D. A. Crawford 2016). The geo and BDL parameters are shown in Tables B1 and B2, respectively.

3.2.2. Spheral

Spheral is an open-source, adaptive, smoothed particle hydrodynamics (SPH) code maintained at Lawrence Livermore National Laboratory (J. M. Owen et al. 1998; J. M. Owen 2010). Spheral has been used for a variety of planetary defense problems, including studies related to the DART impact (M. Bruck Syal et al. 2016; K. M. Kumamoto et al. 2022; J. M. Owen et al. 2022; A. M. Stickle et al. 2022). In this study, we use Spheral's fluid–solid interface SPH (FSISPH) solver, which was designed to model shock problems with significant discontinuities in material properties (J. M. Pearl et al. 2022). The solver has been validated on a suite of shock, multimaterial, elasticity, plasticity, and fracture problems, and here we use the default numerical parameters specified in J. M. Pearl et al. (2022).

The aluminum impactor is modeled with a Tillotson EOS, with the model parameters listed in J. H. Tillotson (1962), while for asteroidal material we use the ANEOS EOS for forsterite (S. T. Stewart et al. 2019) constructed using M-ANEOS (S. L. Thompson & H. S. Lauson 1972; S. L. Thompson 1990; H. J. Melosh 2007; S. L. Thompson et al. 2019). To model the effects of porosity, we use the strain–porosity model of K. Wünnemann et al. (2006) with the thermal correction of G. S. Collins et al. (2011). This approach assumes that compaction is initially elastic up to a threshold strain ε_e, beyond which compaction becomes irreversible and porosity decreases exponentially with strain. In the exponential regime, the compaction exponent κ controls the balance between pore compaction and the compression of the solid matrix (K. Wünnemann et al. 2006, Equations (7) and (8)); as κ gets closer to 1, the material becomes harder to compress. Initial sound speeds for pristine porous material are calculated using the solid sound speed for dunite (6556 m s^{-1}) and a fit to sound speed (c) versus porosity (ϕ) data from L/LL chondrites (G. J. Flynn et al. 2018).

Yield strength is calculated using a modified form of the pressure-dependent approach of G. S. Collins et al. (2004). Yield strength is linearly modified by damage between Y_{i0} and Y_{d0}, with an additional modification for porosity applied by dividing yield strength by current distension (e.g., the initial intact yield strength of the boulders is 850 kPa rather than 1 MPa, as the boulders have 15% porosity). To better compare with other hydrocodes, we plot results from Spheral at the "bulk" value of $Y_{d0,m}$ (e.g., if $Y_{d0,m}$ is 1 kPa for solid material, the "bulk" $Y_{d0,m}$ for a matrix porosity of 40% is 600 Pa).

To model fracture (damage), we use the scale-dependent probabilistic approach of D. E. Grady & M. E. Kipp (1980). The implementation in Spheral is similar to that of W. Benz & E. Asphaug (1994), with modifications detailed in J. M. Owen (2010) and J. M. Owen et al. (2022). Here the material is assumed to contain a set of flaws that become active when their respective threshold strains are surpassed.

The resolution of all of the Spheral simulations presented in the main text is set to be 10 cm at the impact point. The resolution then coarsens in successive shells (radially from the impact site), with size increasing by 1% with each successive shell, resulting in the final asteroid containing ~5.6 million SPH nodes. Each sphere of the impactor is individually discretized with constant resolution, either equal to the maximum resolution of the asteroid or at a level allowing 3 cppr, whichever is more resolved. A summary of parameters varied in Spheral simulations is shown in Table B4.

3.2.3. FLAG

FLAG is an arbitrary Lagrangian–Eulerian (ALE) hydrocode developed and maintained by Los Alamos National Laboratory (D. E. Burton 1992, 1994a, 1994b; J. L. Hill 2017). FLAG has been verified and validated for impact cratering problems and has been used in a variety of planetary science and planetary defense applications (W. K. Caldwell et al. 2018, 2021; W. K. Caldwell 2019; K. M. Kumamoto et al. 2022; A. M. Stickle et al. 2022). FLAG incorporates both analytic and tabular EOSs, multiple constitutive models for solid materials, and damage models (D. E. Burton 1992, 1994a, 1994b). FLAG has multiple remapping and ALE techniques, including adaptive mesh refinement (D. E. Burton 1992, 1994a, 1994b; D. E. Burton et al. 2018).

To model the asteroid materials, we used a Mie–Gruneisen EOS for dunite (N. Heider & T. Kenkmann 2003) with a Johnson–Cook damage model and Von Mises yield criterion. To model porosity, we used a P–α porosity model (W. Herrmann 1969). FLAG's implementation of the Johnson–Cook damage model includes compaction when used with a porosity model. For our strength and damage models, the intact yield strength was varied, rather than the damaged strength. Fully damaged material (damage = 1) had a strength of 0. Material that was partially damaged (0 < damage < 1) had strength between 0 (fully damaged) and the intact yield strength, based on the amount of damage. For all simulations, the computational mesh had varied zone sizes, with the finest resolution having a zone size of 10 cm.

3.3. Key Metrics

3.3.1. Momentum Enhancement Factor

The official definition for β for the DART mission is β_r of A. S. Rivkin et al. (2021) and is given as

$$\beta = \frac{\frac{M}{m_{sc}}\Delta V_T - \boldsymbol{V}_{\infty_{\perp n}}\cdot\hat{e}_T + \boldsymbol{V}_{\infty_n}\boldsymbol{\epsilon}\cdot\hat{e}_T}{\boldsymbol{V}_{\infty_n}(\hat{n} + \hat{\epsilon})\cdot\hat{e}_T}. \quad (5)$$

In this equation, M is the mass of the asteroid; m_{sc} is the mass of the spacecraft; $\boldsymbol{V}$ is the spacecraft velocity, with $\underline{\boldsymbol{V}}_{\infty\perp n}$ being the vector component perpendicular to the asteroid surface normal at the impact site ($\hat{n}$) and $V_{\infty n}$ being the component in the direction of $\hat{n}$; $\hat{e}_T$ is the unit vector in orbital direction; ΔV_T is the change in the asteroid's velocity in the orbital direction; and $\underline{\boldsymbol{\epsilon}}$ is the vector perpendicular to the surface normal with a magnitude equal to the tangent of ξ, where ξ is the angle between the net ejecta momentum and the surface normal. These quantities are all either known prior to impact (m_{sc}, $\underline{\boldsymbol{V}}$, $\hat{e}_T$), measured ($\hat{n}$, ΔV_T), assumed (M), or calculated from simulations ($\underline{\boldsymbol{\epsilon}}$, though $\underline{\boldsymbol{\epsilon}}$ can also be estimated from observations of the ejecta cone). This formulation for β ultimately describes the momentum enhancement in the

direction of the surface normal, and Figure 9 in A. A. S. Rivkin et al. (2021) shows a graphical representation of these vectors and their respective directions.

However, β can be calculated for any direction of interest. For instance, the momentum enhancement in the orbit direction of Dimorphos, β_o, is most easily compared to the velocity change in the orbit direction (e.g., T. S. Statler et al. 2022). In simulations, such as CTH, β can first be calculated along the impact vector (here in the $-z$-direction; a scalar β is calculated and then multiplied by the $-z$ unit vector) and then rotated into the actual orbit velocity direction using the transform matrix (based on the known impact point, impact velocity vector, and orbital velocity vector):

$$\begin{bmatrix} -0.029462 & 0.165336 & -0.985797 \\ 0.984491 & 0.17543 & 0.00000 \\ 0.172942 & -0.970509 & -0.167940 \end{bmatrix}.$$

Once in the orbital velocity direction, the ejecta directions can be determined relative to the surface and β_r can be calculated using Equation (5). In Spheral simulations, the ejecta momentum and the spacecraft momentum in the direction of interest (e.g., the orbital direction) are determined prior to calculating β through Equation (1).

3.3.2. Crater Size

Images from the LICIACube spacecraft show that ejecta were still leaving the surface of Dimorphos several minutes after the DART impact. It is difficult to run shock calculations out to these large timescales without significant modification to the simulation structure. Thus, we estimate crater size based on material motion. We use a velocity criterion, where material with V_z (i.e., velocity in the antispacecraft direction) greater than escape velocity is assumed to be ejected. Here escape velocity is $\sim$9 cm s^{-1}, based on the size and assumed density of Dimorphos ($8.8^{-0.6}_{+0.4}$ cm s^{-1} corresponds to the escape velocity if $\rho_b = 2.4^{-0.3}_{+0.3}$ g cm^{-3}). This cutoff provides an estimate for final crater width, even if the actual transient crater is still forming when the simulation is halted. The reported crater widths are the average of crater width measured in two perpendicular directions. This method was also used in J. M. Owen et al. (2022).

4. Results

4.1. Impact Ejecta Morphology

After the loss of signal from the DART spacecraft, the first confirmations of the success of the DART experiment included the images gathered by LICIACube (E. Dotto et al. 2021, 2024). The LICIACube spacecraft flew by post-impact and returned 426 scientific images; images started 71 s before impact time and ended 320 s after impact. The closest approach occurred about 167 s after impact (E. Dotto et al. 2024). Images returned from LICIACube revealed a complex ejecta curtain with ejecta rays, a wide opening angle, and ejected boulders (Figure 3(a); E. Dotto et al. 2024). Ejecta velocities ranged from a few tens of meters per second to $\sim$500 m s^{-1}. The complex rays extended several kilometers from Dimorphos when LICIACube stopped taking images. These rays were discontinuous, with bifurcations, diffuse clumps, and bends. Further, bright nodes suggest that blocks or boulders are present in the ejecta rays following impact.

The rubble-pile impact simulations of this study all produce complex ejecta structures and rays consistent with what was observed following the DART impact (Figure 3). The wide opening angle of the ejecta cone and the presence of ejecta rays are reproduced regardless of the assumed cohesion, friction, or crush curve (Figures 3(b) and (c)). The ejecta cone is elongated somewhat in the same axis as the solar panels, similar to what was seen following DART's impact (e.g., M. Hirabayashi et al. 2024). The ray structures emerge early in time (Figure 3(c)) and continue to evolve as the crater grows and expands (Figures 3(b) and (d)). The first rays are generated as ejecta from the boulders Atabaque and Bodhran (Figure 3(c)), as these are the first places impacted by the three-sphere impactor configuration (R. T. Daly et al. 2023). Shortly thereafter, as the central sphere (representing the main DART spacecraft) impacts into the target, the matrix material is ejected. Some of this material interacts with the already-formed boulder material rays, while other matrix ejecta move between the remaining surface boulders to create matrix-material-dominated rays (Figure 3(d)).

Simulations into homogenous targets that use the Dimorphos shape model to bound the target do not exhibit these striking rays to the same extent (Figure 4, left). The ejecta curtain is not perfectly symmetrical in these simulations, which is likely due to the irregular surface topography of the shape model at small scales. However, the complex structures seen in simulations including boulders (Figure 3 and Figure 4, right) are not present. This finding is consistent with observations following the Deep Impact mission's impact into Tempel-1, which presented a smoother and more homogenous surface than Dimorphos. Ejecta rays and structure were seen in the images; however, overall, the curtain was much more uniform (P. H. Schultz et al. 2007).

The filamentary ejecta rays seen in LICIACube images indicate that at least one of the mechanisms known to generate ejecta rays is at work: (1) combined ejecta curtains from cluster impacts (P. H. Schultz & D. E. Gault 1985), which also applies to irregular-shaped impactors (F. Pacheco-Vázquez 2019); (2) relatively large target surface topography irregularities (T. Sabuwala et al. 2018; V. Shuvalov 2012); or (3) differences in grain size for granular targets (T. Kadono et al. 2019; J. Ormö et al. 2022). As there is no obvious preferential direction of the observed rays, they are not likely to be an effect of the irregular shape of the impactor (i.e., solar panels for DART, or the three spheres here). Likewise, the DRACO camera does not reveal any topographic surface undulations (e.g., deep impact craters) in Dimorphos (R. T. Daly et al. 2023). Most likely, the filamentary rays stem from the presence of boulders, both on the surface and embedded below, which block ejecta from escaping uniformly, similar to what was seen with the Small Carry-on Impactor (SCI) impact (M. Arakawa et al. 2020) and highlighted in Figure 4 of this paper and Figure 4 in M. Arakawa et al. (2020). This mechanism relies on perturbations caused by large objects (i.e., boulders) on the excavation flow of the small particles in the matrix, which is a gravity-independent process (T. Kadono et al. 2019; J. Ormö et al. 2022). This suggested ray formation mechanism, related to boulders embedded in the target, reveals the likely rubble-pile interior of Dimorphos. If DART had hit a different location on Dimorphos, ejecta rays would still be expected, as the boulder-covered surface appears to be ubiquitous, but the specific structure and orientation would depend on the near-

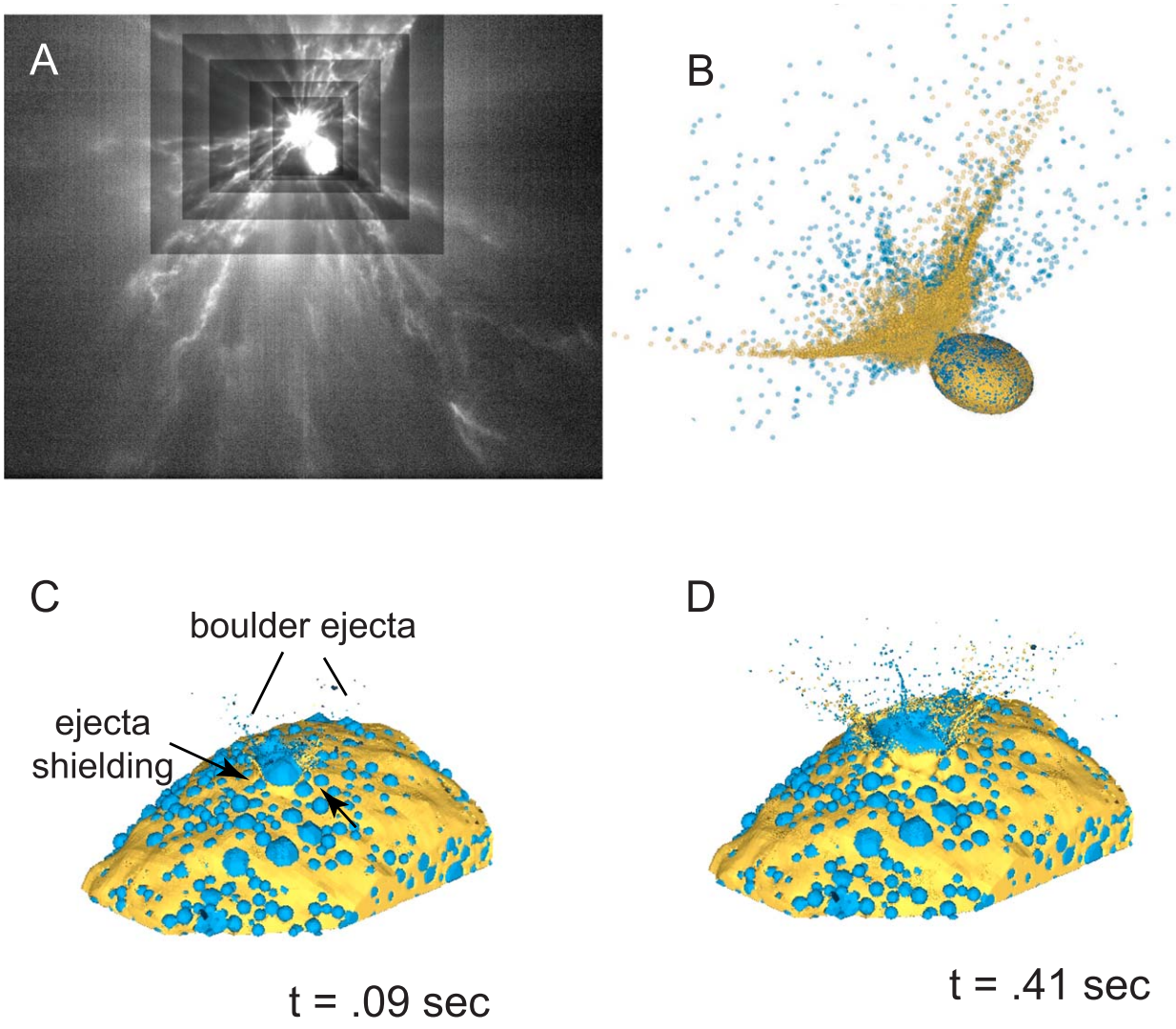

Figure 3. (a) LICIACube image of ejecta following the DART impact (liciacube_luke_l0_1664234207_00000_01). Each rectangle represents a different level of contrast in order to better see fine structure in the rays. (b) Spheral simulation at 4.7 s showing wide ejecta curtain and ejecta rays similar to those seen by LICIACube. (c) CTH simulation showing development of ejecta rays very early in the cratering process (0.09 s) due to interaction of boulder ejecta. (d) CTH simulation showing development of ejecta rays early in the cratering process (0.42 s). These rays are primarily due to heterogeneous surface morphology (boulders and/or slope).

field boulders and topography. This complex ejecta behavior illustrates the importance of including complex (sub)surface morphology when simulating kinetic impactors into asteroids to fully capture the ejecta dynamics.

4.2. Deflection and Momentum Enhancement at Early Times

While the structure of the ejecta is largely similar between different simulations, the magnitude of the deflection supplied by the ejecta in concert with the spacecraft varies widely and is directly associated with material properties. As the deflection is the primary metric regarding the success or failure of a planetary defense deflection mission, it is a vital piece of information to match in our simulations.

The evolution of ΔV over the simulated time (the first tens of milliseconds to seconds) is shown for each simulation in Figures 5(a)–(c). The curves are qualitatively similar, with a sharp increase in ΔV at the beginning of each simulation. The rate of increase then decays over time: the new ejecta produced in the impact are slower, so ΔV asymptotically approaches a constant value. Representative curves for β_o and β_r for 2.4 g cm^{-3} (Figure 5(d)) have the same shape. The difference between β_o and β_r is minor relative to the differences associated with material properties.

A general sense of the extrapolated deflection magnitudes can be gained using a simple logarithmic fit of the form

$$\Delta V = a \ln(bt + c) + d, \tag{6}$$

where t is time and a, b, c, and d are fitting constants. This functional form generally fits early deflection data quite well, though its application is necessarily limited since the function does not have an asymptote (i.e., deflection magnitude increases indefinitely with time). In all cases shown in Figure 5, the β curves appear to approach values greater than 2, indicating that the momentum of the ejecta contributes more to the deflection than the incident spacecraft momentum. Variations in β between models at any given time indicate the effects of material properties on net ejecta momentum.

Within any given code, ΔV follows predictable trends with any given material parameter. Larger deflection magnitudes are observed for smaller cohesion values and smaller coefficients of friction (Figures 5(a)–(c), Figure 6(a)), though the effect of

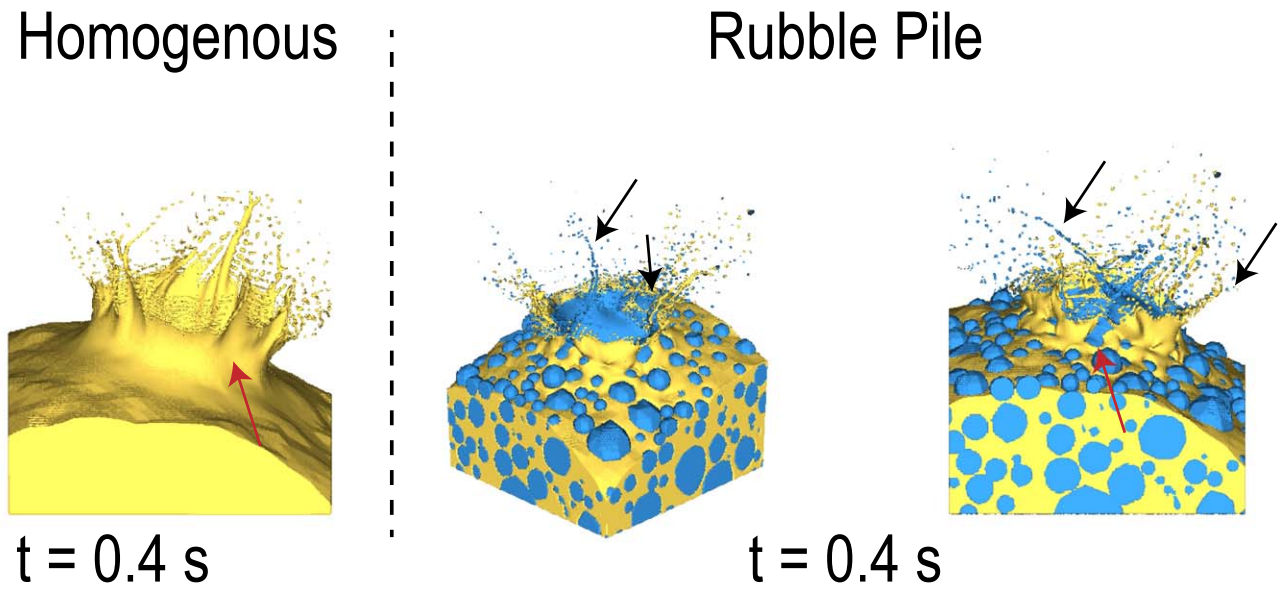

Figure 4. Left: crater and ejecta formation for an impact of three aluminum spheres into a 10 Pa homogeneous target with a coefficient of friction $f_{i,m} = 0.6$ and $\rho_b = 2.1$ g cm^{-3}. The surface matches the shape model of Dimorphos. Snapshot shown at 0.4 s. Right: crater growth and ejecta ray formation in the time immediately following a DART-like impact into a rubble-pile target; snapshot at 0.4 s. The simulations show results of the impact of three aluminum spheres into a 10 Pa target with a coefficient of friction $f_{i,m} = 0.6$ and $\rho_b = 2.1$ g cm^{-3}. Two different views of the evolving ejecta are shown. The earliest ejecta are released from Atabaque and Bodhran (in blue). Additional material begins to interact as the crater grows outward into the matrix (yellow; here, anything with size <2 m). Ejecta interact and rays cross each other in complicated patterns, highlighted by black arrows. The red arrows show the ejecta near the surface; the homogenous target has much smoother ejection compared to the rubble pile, where the near-surface ejecta is turbulent owing to interactions with boulders. The area shown is a 20 m × 20 m cutout of the asteroid. The animation is 4 s long and includes additional frames to those shown in the static figure. The animation shows the initial impact of the three-sphere DART representative impactor followed by the ejecta evolution from a homogenous target (left) and two views of the rubble-pile target (right). The ejecta evolution following impact into a rubble pile is more turbulent, especially near the surface, compared to a homogenous target, resulting in complicated and interacting ray structures and ejecta shielding. Different materials are represented by each color: dark blue represents the DART spacecraft, light blue represents Dimorphos boulders, and yellow represents Dimorphos matrix material.

(An animation of this figure is available in the online article.)

coefficient of friction (Figure 6(a)) is significantly smaller than that seen for different cohesion (Figure 5).

As seen in Figures 6(b) and (c), larger deflection magnitudes are also correlated with larger crush strengths (i.e., larger pressures required to completely close pore space). This is because the cratering process involves compaction in addition to ejection (K. R. Housen et al. 1999). In our simulations (as well as the DART experiment), part of the kinetic energy into the target is dissipated by compaction and crushing of pore space, which results in less total ejecta and reduced ejecta velocities. Deflection and momentum enhancement are thereby reduced. Thus, the initial porosity and the detailed definition of the crush curve have significant influences on deflection, as they govern the partitioning of energy between crushing and ejection.

Precisely modeling the role of microporosity in CTH is accomplished by using the P–α model, which takes pore compaction into account, separating the calculation of compression and pore collapse. We examine the effects of varying the pore compaction pressure (P_s) in the P–α model for our Dimorphos target material. We tested two pore compaction scenarios for the case where the intact matrix yield strength $Y_{i,m} = 500$ Pa, matrix friction coefficient $f_{i,m} = 1$, and density $\rho_b = 2.1$ g cm^{-3} (15 cm grid resolution): the nominal granite-like value of $P_s = 213$ MPa used throughout the majority of the simulations, and a weaker shale-like value of $P_s = 21.3$ MPa. Figure 6(b) shows that decreasing the pore compaction ($\boldsymbol{P_s}$) by an order of magnitude results in a ∼25% reduction in ΔV and β at early times (350 ms), which is likely to increase at longer simulation times. This decrease illustrates the importance of the porosity model and crush curve parameters, because it controls the peak pressures experienced in the shock wave, as well as how the energy dissipates in the target.

In Spheral, the effect of the crush curve parameters on deflection was investigated by examining three different values for κ (0.90, 0.99, and 0.9999) on our simulations with $\rho_b = 2.4$ g cm^{-3}. Smaller values of κ result in larger crush strengths for otherwise-identical simulations, which in turn results in larger values for ΔV and β, as more energy is spent ejecting material rather than crushing it further (Figure 6(c)). This effect manifests in the cumulative ejecta curves of each simulation, with curves from simulations with larger κ broadly being offset to lower velocities (Figure 7), though total ejecta masses at late times may vary.

Simulations largely overpredict the deflection for the least dense case ($\rho_b = 2.1$ g cm^{-3}) and are closer in value to the observed deflection for $\rho_b = 2.4$ g cm^{-3} or higher. Several of our simulations, especially for lower- and middle-density materials, have reached the target velocity change by 1–1.5 s, and the gradient of the velocity curves at these times indicates that a great deal more ejecta are likely to contribute to ΔV at later times. Multiple sets of material properties appear consistent with the observed deflection at early times.

4.3. Estimating Crater Size

Determining the final crater size and morphology in impact simulations is complex because it usually requires long simulation times, and the transition between crater growth and collapse can be complicated by material strength properties. For impacts into high-strength, or low-gravity, targets,

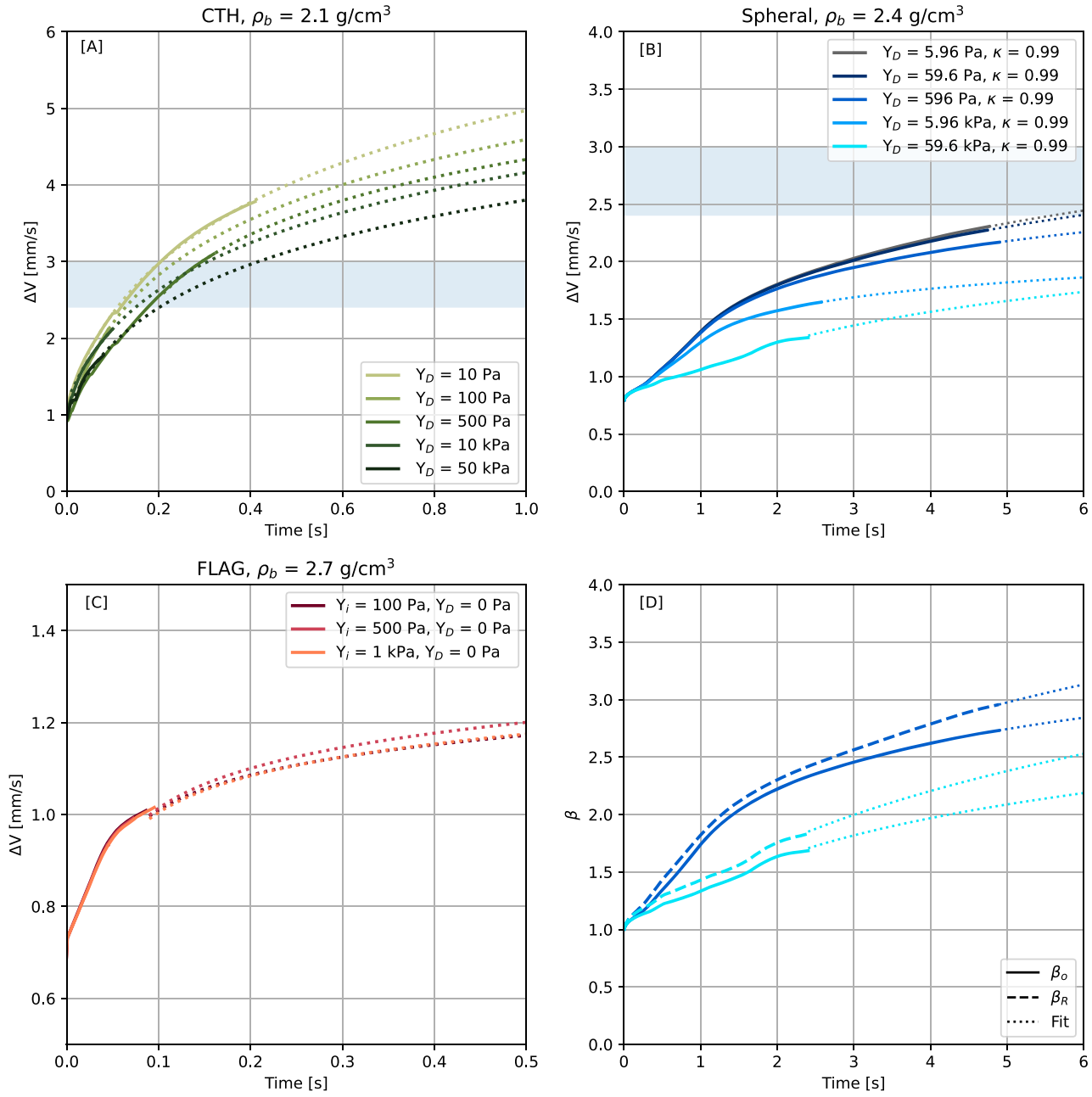

Figure 5. Representative simulation results from this study. In all panels, the dotted lines signify a logarithmic fit to the data, and the solid or dashed colored lines are values directly from the simulations. (a–c) ΔV as a function of time for a subset of simulations. (a) ΔV as a function of time from CTH simulations with $\rho_b = 2.1$ g cm^{-3}. (b) ΔV as a function of time from Spheral simulations with $\rho_b = 2.4$ g cm^{-3}. (c) ΔV as a function of time from FLAG simulations with $\rho_b = 2.7$ g cm^{-3}. The strength in these simulations is defined as $Y_{d,m} = 0$ Pa and $Y_{i,m} = 100$ Pa, 500 Pa, and 1 kPa. (d) Calculating β in the orbital direction and the surface normal direction (A. S. Rivkin et al. 2021) shows only subtle differences. The blue shaded regions in panels (a) and (b) show the measured ΔV for the DART mission with 3σ standard deviation.

crater collapse may be negligible because the strength of the material can support somewhat-steepened walls. In low-strength or large-scale/high-gravity cratering situations, defining this transition is more complicated because the transition from outward excavation flow to inward modification flow does not occur at the same time in every direction. For example, in most cases the crater depth reaches a maximum before the crater diameter (E. P. Turtle et al. 2005). D. Elbeshausen et al. (2009) found that the end of crater excavation (and the beginning of modification) coincides approximately with the time when the (first) maximum in crater volume is reached. For very low strength target material, final collapse may increase crater volume for the final crater. In the case of Dimorphos, this is likely a complicated interplay of low gravity and moderate to low strength.

Using $V_z > V_{\rm esc}$ as our main criterion for determining what material will eject at late times, we estimate the diameter for the final transient crater at several points in our simulations (Figure 8, Tables A2–A4). In general, estimated final crater diameters begin to stabilize around 500 ms (Figure 8(c)). For simulations with lower cohesive strengths (<1 kPa), the estimated crater diameter continues to grow slightly as more material is ejected. For simulations with higher cohesive strengths (>1 kPa), estimates for the final crater diameter

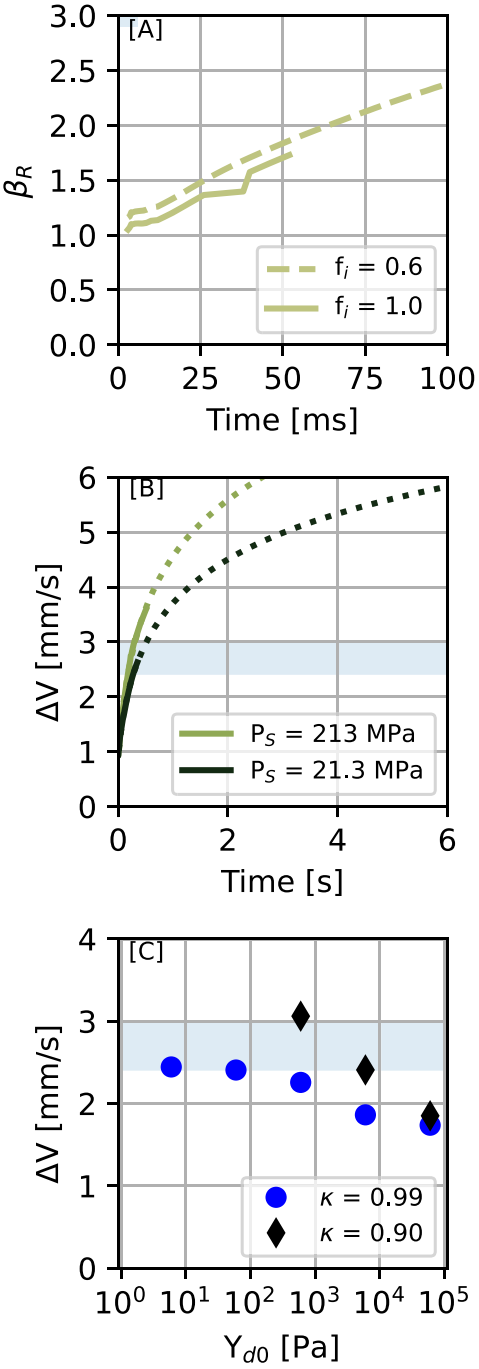

Figure 6. (a) β_R vs. time for two CTH simulations with the same cohesive strength (Y_d) but different friction coefficient. (b) ΔV vs. time for two CTH simulations with different crush curve parameters. The blue shaded region shows the measured ΔV for the DART mission with 3σ standard deviation. P_s is the pressure where all porosity is crushed out, the "pore compaction pressure." (c) ΔV at 6 s based on Spheral simulations with $\rho_b = 2.4$ g cm^{-3} for three values of κ. Note that κ is the compaction exponent that controls the balance between pore compaction and the compression of the solid matrix (see Section 3; K. Wünnemann et al. 2006); as κ gets closer to 1, the material becomes harder to compress. A logarithmic fit is used to extrapolate ΔV for simulations that did not reach 6 s. The blue shaded region shows the measured ΔV for the DART mission with 3σ standard deviation.

decrease as the higher strength slows material and keeps it from escaping. Final estimated crater diameters from simulations past 100 ms range from ~15 m for cases with the highest Y_d to 50–60 m for cases with the lowest Y_d.

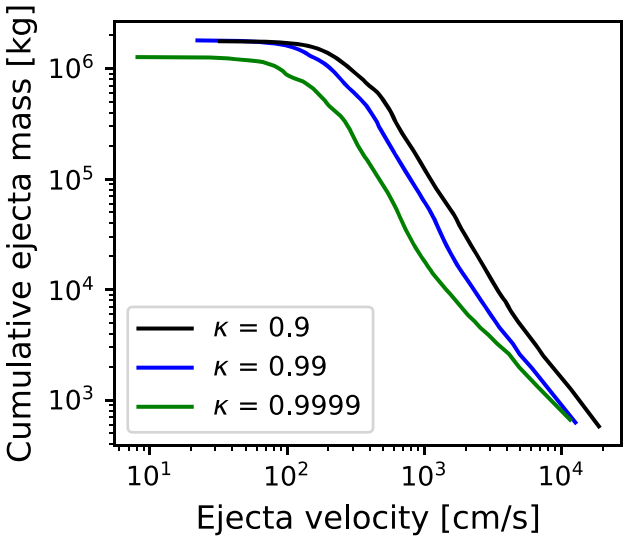

Figure 7. Cumulative ejecta mass–velocity distributions for Spheral simulations with $Y_d = 596$ Pa at maximum simulation time and for three different values for the epsilon–alpha compaction exponent, κ (K. Wünnemann et al. 2006). Simulation IDs in Table A1 are 4.00, 4.01, and 4.02.

Analysis of the crater formation and ejecta suggests that these simulations, if run longer, would produce ejecta masses consistent with the observations following DART. At the time at which simulations were halted, ejecta mass is still growing approximately linearly and significant material is still moving with velocities >100 cm s^{-1}, even for simulations with higher assumed strength values (e.g., 100 Pa–1 kPa). Using the $V_z > V_{esc}$ criterion from the crater estimate, we can calculate the total mass of material we expect to escape Dimorphos. The extrapolated ejecta masses for our simulations are 8.9×10^5 kg to 3.3×10^7 kg (Figure 8(d), Table A1). Estimates for most of the measured simulations are the same order of magnitude as estimates for the total mass of ejected material from the DART impact based on the brightening of the Didymos system after impact, i.e., (1.3 ± 0.1)–6.4×10^7 (A. Graykowski et al. 2023; D. Jewitt et al. 2023; N. X. Roth et al. 2023).

4.4. Self-consistent Extrapolation of Deflection to Late Times

When comparing simulations to the DART experiment, we can compare simulation results to observations that occurred minutes (LICIACube images; E. Dotto et al. 2024) to hours and days to weeks (J. Y. Li et al. 2023; ejecta mass and total deflection) after the impact. The logarithmic fit employed earlier is a helpful metric at early times, but its application to predictions beyond a few seconds post-impact is tenuous at best. Pre-impact simulations suggest that changes in ΔV and β are small after several seconds when cohesive strengths are on the order of kPa or more (J. M. Owen et al. 2022; A. M. Stickle et al. 2022). However, simulations suggest that lower-strength or strengthless targets continue to evolve for a much longer period of time (S. R. Schwartz et al. 2016; A. F. Cheng et al. 2022; S. D. Raducan & M. Jutzi 2022). Similar behavior was also seen during the Hayabusa-2 SCI impact (M. Arakawa et al. 2020). Unfortunately, impact simulations can be limited in their ability to run to later times (i.e., once the shock wave decays into elastic waves, or longer crater formation times in the gravity cratering regime) without handoffs to longer time integration schemes (e.g., M. Jutzi et al. 2022; S. D. Raducan & M. Jutzi 2022), which are beyond the scope of this study.

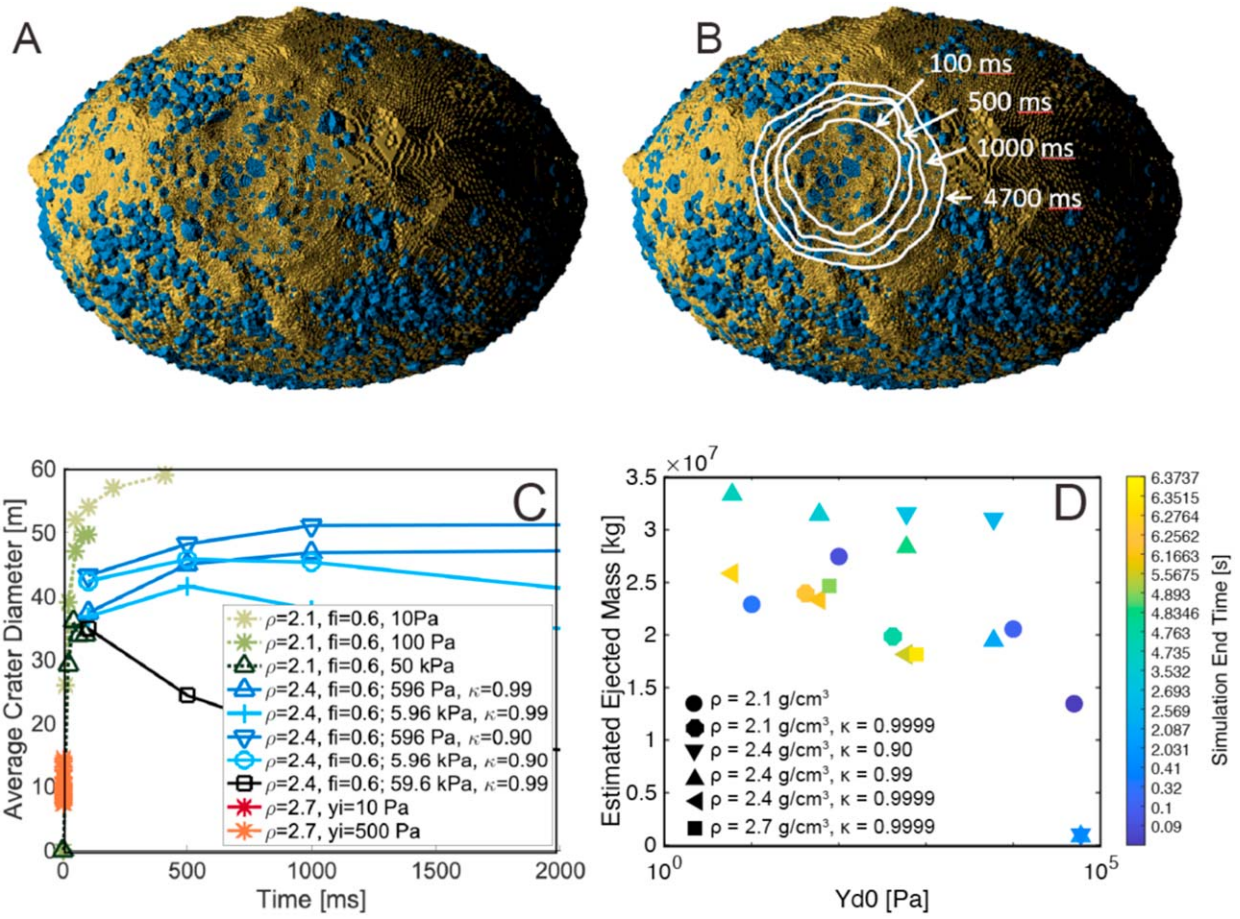

Figure 8. Crater size estimates from impact simulations. (a) Top-down view of a Spheral simulation 4.7 s after impact ($\rho_b = 2.4$ g cm^{-3}, $Y_{d0,m} = 5.96$ Pa, $\kappa = 0.99$) with all material traveling away faster than escape velocity removed. (b) The same simulation as in panel (a), but with contours showing how the estimated final crater rim increases with time. Even at maximum simulation time, the crater is still getting slightly larger. (c) Average crater diameter as a function of time for a subset of simulations at three different target densities. Two different crush curves are shown for a representative Spheral simulation ($\kappa = 0.99$ and 0.90). (d) Estimated crater ejecta mass for these simulations matches the estimated ejecta mass from the DART impact. The color of each symbol corresponds to the simulation end time, and the shape of the symbol represents specific codes and initial parameters. Estimates of ejecta mass from observations following impact are (1.3–6.4) $\times 10^7$ (A. Graykowski et al. 2023; D. Jewitt et al. 2023; N. X. Roth et al. 2023). The data for panels (c) (simulated crater diameters) and (d) (simulated crater ejecta mass) are available as data behind the figure in the online Journal.

(The data used to create this figure are available in the online article.)

We propose an alternative approach to a self-consistent extrapolation to late times using the cumulative ejecta mass–velocity distribution for each simulation (Figure A1) and the estimated total ejecta mass at the maximum simulation time (Figure 8(d)). This process is shown schematically in Figure 9(a). Cumulative ejecta mass–velocity distributions for hypersonic impacts are commonly represented by power laws (e.g., K. A. Holsapple & K. R. Housen 2012). We fit our distributions with a power law ($y = Ax + b$ in log–log space) over a velocity range of either 10^3–10^4 cm s^{-1} (CTH) or $10^{2.8}$–$10^{4.5}$ cm s^{-1} (Spheral), where distributions appear to match a power law. We then extrapolate the power law to lower velocities until we reach a cumulative mass equal to the estimated total ejecta mass from the $V_z > V_{esc}$ criterion (e.g., Figure 9(a)). This extrapolation is detailed in this section. By taking the integral under this power law, we can calculate the total momentum of the ejecta and thus estimate β. For this analysis, we calculate β in the antispacecraft velocity direction ($\beta_z \sim \beta_0$; e.g., Figure 5(d)).

The results of this extrapolation are shown in Figure 9(b) for a subset of the simulations in this study. We expect that the total ejecta momentum calculated in this way will be an overestimate because our simulations do not include gravity, so we also show results including a correction for the influence of gravity following K. A. Holsapple & K. R. Housen (2012; open symbols in Figure 9). In general, with or without a correction for gravity, the calculated values of β_z from our extrapolations are much larger than the final values of β_z at maximum simulation time because significant material mass is expected to be ejected in all but the strongest cases (100 kPa). Variation of the extrapolated β_z with either cohesive strength or crush strength follows the relationships observed at simulated times, with lower cohesive strengths and higher crush strengths corresponding to larger values of β_z.

Our proposed extrapolation is strongly dependent on how closely the cumulative ejecta mass–velocity distributions follow a power law and on the estimated total ejecta mass. Deviations of the ejecta distributions from a power law in our simulation results are attributed, at least in part, to the curvature of the surface of Dimorphos (M. Hirabayashi et al. 2024), as well as to the mixture of matrix and boulder material present in the ejecta. These uncertainties are difficult to quantify without running the simulations further, but the former especially will decrease estimates for the late-time β_z. Simulations in other

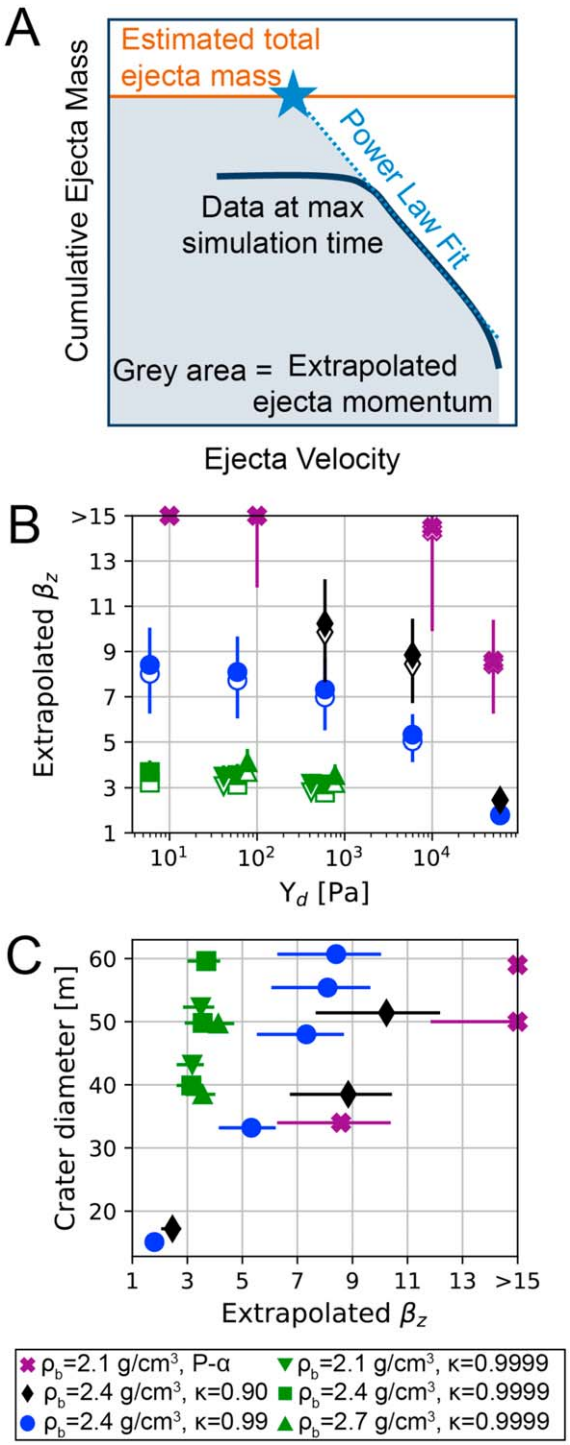

Figure 9. (a) A schematic representation of the extrapolation method. The figure is shown with logarithmic axes; thus, the portion of the ejecta distribution that appears linear can be fit with a power law. (b) Extrapolated β_z vs. Y_{d0} for representative CTH and Spheral simulations. Uncertainties on the extrapolated β_z represent ±50% ejecta mass. This value was chosen to illustrate the sensitivity of extrapolated β_z to total ejecta mass. The open symbols show the same simulations with a gravity correction following K. A. Holsapple & K. R. Housen (2012). Many points overestimate the calculated β from the DART experiment (A. F. Cheng et al. 2023), suggesting that the material properties and strength models chosen for those simulations may not be a good fit to Dimorphos. For densities of ρ = 2.1–2.7 g cm^{-3}, Cheng et al. calculate β = 2.2–4.9. (c) Crater diameter vs. extrapolated β_z. Y_{d0}, ρ_b, and choice of crush curve all have significant effects on the crater diameter for a given value of β_z.

studies of the DART impact, however, suggest that the cumulative ejecta mass–velocity distributions continue to follow a power law at hundreds of seconds, when the slowest ejecta are moving slower than escape velocity (S. D. Raducan et al. 2024). The effect of the estimate for the total ejecta mass is simpler to explore. Because we calculate our estimated ejecta masses from the criterion of $V_z > V_{esc}$ at times of milliseconds to seconds after impact, we may be underestimating the total ejecta mass for the weaker cases and overestimating ejecta for the stronger cases in the same manner as crater diameter. In addition, while Figure 8(c) indicates that the crater diameter is stabilizing for many of the simulations, the crater floor is generally still moving down at maximum simulation time for $Y_{d0} < 1$ kPa, suggesting that the total ejecta mass is underestimated by the velocity criterion. To demonstrate the effect of the ejecta mass estimate on β_z, the uncertainty bars in Figure 9(b) show a range for β_z from increasing or decreasing total ejecta mass by 50%.

Our results demonstrate that a variety of models and material property combinations can reproduce the β observed in the DART impact (i.e., 2.2–4.9 depending on density; A. F. Cheng et al. 2023). Crush curves with higher crush strengths result in a greater proportion of the impactor's kinetic energy going toward ejecting material rather than compacting it, and so a relatively large value of Y_{d0} (kPa to tens of kPa) is required to reproduce the β observed in the DART impact. For crush curves with lower crush strengths, such as those with $\kappa = 0.9999$, lower cohesive strengths in the range of Pa to tens of Pa are needed to match the DART β.

Other observations from the DART impact may reduce the range of possible results. For instance, the total ejecta masses predicted by simulations with cohesive strengths in the range of tens of kPa are 1.95×10^7 kg to $\sim 3 \times 10^7$ kg. These are at the low end of estimates for total ejecta mass based on observations, $(1.3–6.4) \times 10^7$ kg (A. Graykowski et al. 2023; D. Jewitt et al. 2023; N. X. Roth et al. 2023). Simulations with the highest cohesive strengths (~60 kPa) have 8.97×10^5 kg to 1.35×10^6 kg of ejecta, falling outside of the predicted range of ejecta mass. As another example, LICIACube-observed ejecta are still being produced when the cubesat passed by Dimorphos ~3 minutes after the impact (J. D. P. Deshapriya et al. 2023; E. Dotto et al. 2024). A. F. Cheng et al. (2023) suggest that these ejecta timelines mean that the impact strength of Dimorphos is <5 kPa, and likely closer to 5–500 Pa; this is largely consistent with the results shown above. We can also use scaling rules based on impacts into homogeneous targets (e.g., K. A. Holsapple & K. R. Housen 2007) to calculate an estimate for crater formation time as a function of cohesive strength, though there is expected variance resulting from the presence of boulders in our simulations. In Figure 10, we use scaling rules and calibrations from K. A. Holsapple & K. R. Housen (2007) for highly porous material in the strength regime and dry sand in both the gravity and strength regimes to predict both crater size and crater formation time. The predicted crater radii from our simulations are shown in Figure 10(a), and the time of LICIACube's observations is shown as a band in Figure 10(b). The scaling rules we examine suggest that cohesive strengths of ~100 Pa or less are required for ejecta production, and therefore crater excavation, to still be occurring during the LICIACube observations. Further, telescopic observations following the DART impact suggest that the impact may have significantly altered the shape of Dimorphos (e.g., S. P. Naidu et al. 2024; P. Pravec et al. 2024); this reshaping is likely due to a

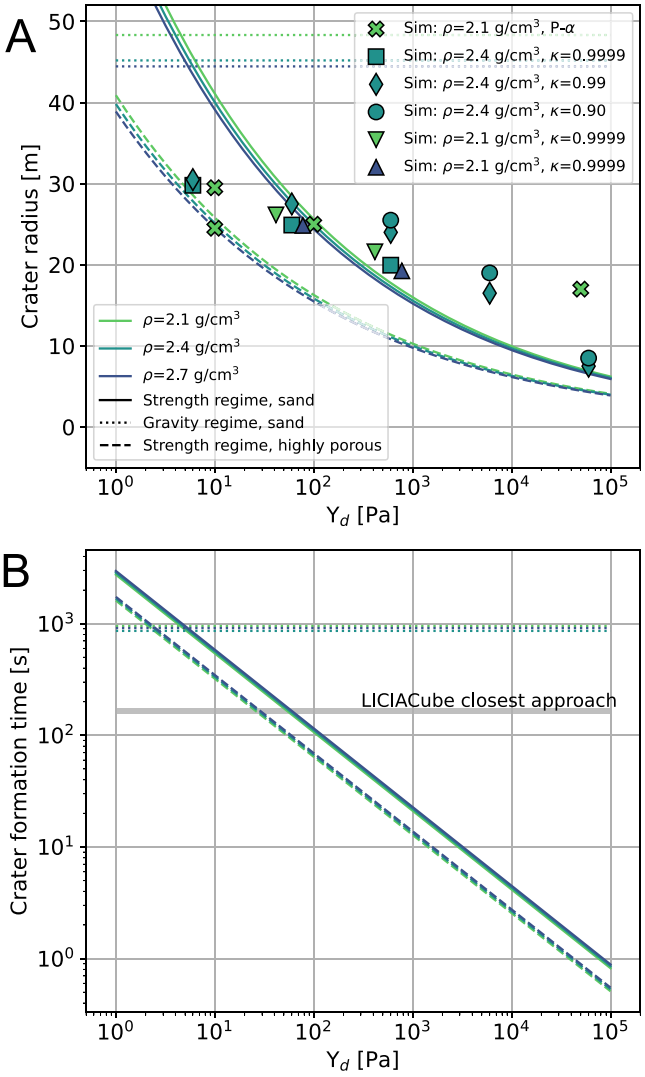

Figure 10. Comparing simulation results (symbols) to the scaling rules (lines) of K. A. Holsapple & K. R. Housen (2007). The colors of the lines and points indicate different bulk densities for Dimorphos; the dashed vs. solid lines represent different regimes. (a) Crater radius as a function of Y_{d0}. (b) Crater formation time as a function of Y_{d0}. The gray line is the time of LICIACube's closest approach. If ejecta were still being actively produced at this time, scaling rules suggest cohesive strengths of ∼100 Pa.

crater with a large diameter compared to the moon's size. These simulation results are generally consistent with this observation as well, though the observed reshaping suggests that the larger-diameter craters are more likely (e.g., green and blue points in Figure 9 and strengths less than ∼5 kPa in Figure 8). Our extrapolations here do not account for material moving at speeds less than escape velocity and so may also be an underestimate of true final crater size and morphology because material may move out along the surface of the body and not be ejected following the impact.

Additional geometric factors that were estimated for these simulations may also play a major role in matching the DART impact. The simulated versions of Atabaque and Bodhran are 6 m diameter spheres and therefore likely bigger relative to their counterparts on Dimorphos. Any effects of these outsized boulders may be exacerbated by our approximation of the spacecraft as three solid spheres of aluminum. The three-sphere impactor overestimates β compared to a more detailed model of the DART

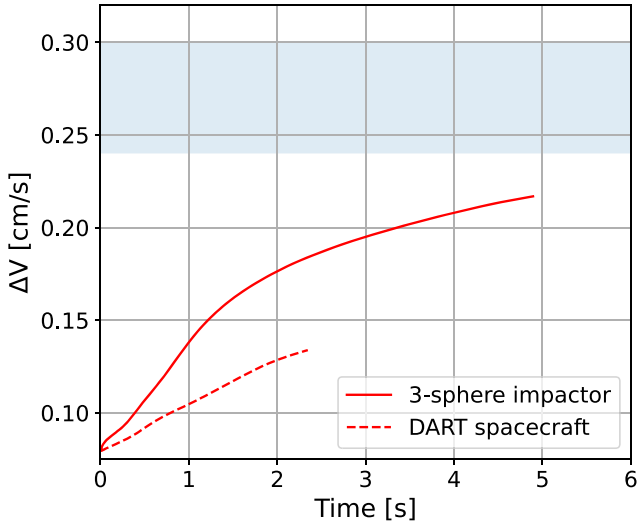

Figure 11. ΔV vs. time for two simulations with different impactor geometries. Aside from the geometry and impactor material, the simulations are otherwise identical (Spheral, $\rho_b = 2.4$ g cm^{-3}, $Y_d = 596$ Pa, $\kappa = 0.99$). The blue shaded region indicates the ΔV estimated for the DART impact.

spacecraft when impacting a homogeneous target (J. M. Owen et al. 2022), and this overestimation is larger in our models with boulders (Figure 11), likely because of the impact of the solid aluminum wing spheres on the boulders in our simulations compared to the thin, expansive solar panels on the DART spacecraft. This result suggests that additional combinations of density, cohesive strength, and crush curves, with lower density or either lower cohesive strengths or higher crush strengths, would be needed to shift from three-sphere-impactor simulations that match the DART experiment to DART-impactor simulations that also match experimental data. Future simulations will examine these effects in greater detail.

5. Implications and Predictions for Hera

Complex impact models, under some assumptions about structure and material behaviors, can successfully simulate the DART impact. While the models cannot determine what the actual physical strength was, the DART experiment showed that we can successfully model a real impact into a "weak" boulder-covered asteroid (or a rubble-pile asteroid), which are expected to be common among possible Earth impactors.

Despite remaining uncertainties, initial models provide important information about the DART impact and the properties of Dimorphos that can be tested by the upcoming European Space Agency Hera mission to the Didymos system (P. Michel et al. 2022). As seen in previous work (e.g., A. M. Stickle et al. 2022, and references therein), matching material properties to deflection is degenerate (Figure 9(b)). The best matches between extrapolated deflections and the deflection measured in DART have a variety of properties, with cohesive strengths ranging from Pa to tens of kPa. Adding LICIACube observations and estimates of total ejecta mass further constrains the solution set, suggesting that lower cohesive strengths (<500 Pa) and lower crush strengths are required, consistent with other studies (e.g., S. D. Raducan et al. 2024). These simulations predict crater diameters in the range of 40–60 m (Figure 9(c)). Additional factors, including the geometric simplifications utilized for both the spacecraft and the impact-site boulders, may imply even lower cohesive strengths than those studied here owing to decreased early ejecta mass and velocity.

Simulated crater size estimates (Figure 8) therefore provide a crucial comparison metric for Hera (P. Michel et al. 2022). When Hera arrives, the measurement it makes of the DART impact crater will be one of the most important measurements to help constrain the material properties of Dimorphos. However, impact simulations generally provide estimates of transient crater size, which will not be the same as the crater measured by Hera. Further, additional modification or collapse may occur in the intervening time from DART's impact to Hera's arrival. The magnitude of this modification will depend on the unknown material properties of the asteroid, the interior structure, and whether the initial crater is a large fraction of the asteroid body size, as well as any potential tumbling motion that may have been excited by DART's impact. However, it is likely that it will still be possible to determine the general magnitude of the crater diameter (e.g., 10 m vs. 50 m vs. 100 m), which can be compared to simulations. Figure 9(c), which compares the extrapolated β_z to the crater size, clearly demonstrates the diagnostic ability of crater size when combined with the observed velocity change (and inferred β) from the experiment. The measurement of crater size, in combination with measurement of Dimorphos's mass (and thus the bulk density), will allow us to assess our simulations and provide the information needed to make the DART impact experiment the first full-scale planetary defense simulation validation exercise, in addition to being humanity's first test of a planetary defense mitigation mission. Additional measurements from Hera—for example, radar information revealing details about the interior structure—will provide additional avenues to further constrain other material properties and strength behaviors.

DART was a very successful test of a kinetic impactor. However, it was an experiment that also generated a new set of questions about the details of kinetic impactors and how to best simulate asteroid impacts in the future. Many uncertainties remain about Dimorphos and its properties, thereby complicating the model comparisons and analysis. Furthermore, an impact that was observed from beginning to end with high-speed cadenced data (e.g., similar to the Deep Impact mission) would provide a means to allow adjustment of models with enough fidelity to apply them to a range of impact scenarios going forward. Ideally, information about early- and late-time ejecta behavior, any vapor plume or jetting, the transient crater size, and ejecta morphology from initial impact through crater formation should be collected. All these stages affect the energy and momentum transferred to the target. DART should thus be seen as the first but by no means the last kinetic impact test.

Data Availability Statement

The data for Figure 8, panels (c) (simulated crater diameters) and (d) (simulated crater ejecta mass), are available as data behind the figure in the online Journal. The specific PDS4 data products from T. Daly et al. (2023) used in this work include the version 3.0 of Dimorphos shape model produced using SPC: urn:nasa:pds:dart_shapemodel:data_derived_dimorphos_model_v003::1.0

Acknowledgments

This work was supported by the DART mission, NASA Contract No. 80MSFC20D0004. Portions of this work were performed under the auspices of the U.S. Department of Energy by Lawrence Livermore National Laboratory under Contract DE-AC52-07NA27344. LLNL–JRNL-853805. Portions of this work were supported by the Advanced Simulation and Computing (ASC) Verification and Validation Planetary Defense Program at Los Alamos National Laboratory. Los Alamos National Laboratory, an affirmative action/equal opportunity employer, is operated by Triad National Security, LLC, for the National Nuclear Security Administration of the U.S. Department of Energy under contract 89233218NCA000001. LA-UR-24-25758. MP, AL, and FT acknowledge financial support from Agenzia Spaziale Italiana (ASI, contracts No. 2019-31-HH.0 and No. 2022-8-HH.0). The work by J.O., S.R., and G.S.C was supported by grant PID2021-125883NBC22 by the Spanish Ministry of Science and Innovation/State Agency of Research MCIN/AEI/10.13039/501100011033 and by "ERDF A way of making Europe." The work by J.O., I.H., S.R., R.L., M.J., and K.W. was supported by the Spanish Research Council (CSIC) support for international cooperation: I-LINK project ILINK22061.

Appendix A
Summary of Simulations

This appendix summarizes simulation parameters and selected results for the simulations used in this study (Tables A1–A4 and Figure A1).

Table A1
Summary of Results from Simulations for This Study

Code	Sim ID	ρ_b (g cm^{-3})	$Y_{d,m}$ (Pa)	$f_{d,m}$	Max Res (cm)	ΔV (orbit) at t_{max} (mm s^{-1})	β_o at t_{max}	β_r at t_{max}	Crater width at t_{max} (m)	t_{max} (ms)	Projected Ejecta Mass (kg)
CTH	…	2.1	10	0.6	15	3.69	3.73	4.15	59	410	2.30E7
CTH	…	2.1	10	0.6	7.8	2.98	3.25	3.47	49	120	1.73E7
CTH	…	2.1	10	1	15	0.82	1.76	1.73	52	52	…
CTH	…	2.1	100	0.6	10	2.11	2.26	2.30	50	100	2.75E7
CTH	…	2.1	500	0.6	3	1.25	1.43	1.38	…	13	…
CTH	…	2.1	500	1	3	1.25	1.43	1.39	…	10	…
CTH	…	2.1	500	0.6	5	1.41	1.61	1.58	…	20	…
CTH	…	2.1	500	1	5	1.21	1.33	1.33	…	10	…
CTH	…	2.1	500	0.6	10	2.24	2.42	2.63	32	150	…
CTH	…	2.1	500	1	10	2.24	2.42	2.62	32	150	…
CTH	…	2.1	500	0.6	15	3.37	3.36	4.24	56	500	…
CTH	…	2.1	500	1	15	3.59	3.57	4.55	57	510	…
CTH	…	2.1	10000	0.6	15	1.9	2.9	3.12	…	320	2.06E7
CTH	…	2.1	50000	0.6	10	1.78	1.90	1.89	34	90	1.35E7
CTH	…	2.7	10	0.41	4	3.13	3.94	4.24	46	85	…

Table A1
(Continued)

Code	Sim ID	ρ_b (g cm^{-3})	$Y_{d,m}$ (Pa)	$f_{d,m}$	Max Res (cm)	ΔV (orbit) at t_{max} (mm s^{-1})	β_o at t_{max}	β_r at t_{max}	Crater width at t_{max} (m)	t_{max} (ms)	Projected Ejecta Mass (kg)
CTH	…	2.7	10	1	4	1.45	1.71	1.77	33	20	…
FLAG	…	2.7	$Y_{i,m} = 1000$	…	10	1.04	1.58	…	14	130	…
FLAG	…	2.7	$Y_{i,m} = 10$	…	10	0.91	1.38	…	9	53	…
FLAG	…	2.7	$Y_{i,m} = 100$	…	10	1.02	1.56	…	14	113	…
FLAG	…	2.7	$Y_{i,m} = 500$	…	10	0.96	1.47	…	11	70	…
Spheral	1.00	2.4	5.96	0.6	10	2.31	2.90	3.14	61	4763	3.34E7
Spheral	1.02	2.4	5.96	0.6	10	1.66	2.05	2.24	60	6512	2.59E7
Spheral	2.00	2.4	59.6	0.6	10	2.27	2.86	3.09	55	4735	3.15E7
Spheral	2.02	2.4	59.6	0.6	10	1.62	2.00	2.19	50	6425	2.34E7
Spheral	2.02.1	2.1	41.5	0.6	10	1.82	1.96	2.11	52	6274	2.40E7
Spheral	2.02.2	2.7	77.7	0.6	10	1.61	2.25	2.43	50	5564	2.47E7
Spheral	4.00	2.4	596	0.6	10	2.17	2.73	2.96	48	4893	2.84E7
Spheral	4.00D	2.4	596	0.6	10	1.34	1.63	1.73	…	2345	…
Spheral	4.01	2.4	596	0.6	10	2.78	3.51	3.70	51	3532	3.16E7
Spheral	4.02	2.4	596	0.6	10	1.50	1.85	2.02	40	6322	1.82E7
Spheral	4.02.1	2.1	415	0.6	10	1.65	1.78	1.88	43	4835	1.99E7
Spheral	4.02.2	2.7	777	0.6	10	1.50	2.09	2.29	39	6372	1.82E7
Spheral	4.11	2.4	596	0.46	5	2.93	3.68	3.82	…	1612	…
Spheral	4.12	2.4	596	0.46	10	2.57	3.23	3.39	…	1779	…
Spheral	4.13	2.4	596	0.46	15	2.23	2.80	2.97	…	1759	…
Spheral	5.00	2.4	5960	0.6	10	1.65	2.07	2.19	33	2569	1.95E7
Spheral	5.01	2.4	5960	0.6	10	2.26	2.83	2.94	38	2693	3.11E7
Spheral	6.00	2.4	59600	0.6	10	1.31	1.65	1.78	15	2087	8.97E5
Spheral	6.01	2.4	59600	0.6	10	1.77	2.22	2.40	17	2031	1.07E6

Table A2
Average Crater Diameter versus Time for Select Spheral Simulations

Simulation	Crater Diameter (m) at 100 ms	500 ms	1000 ms	t_{max}[a]
Spheral 1.00	37.6	46.0	49.7	60.7
Spheral 2.00	37.2	45.9	49.5	55.4
Spheral 4.00	37.4	45.0	46.8	48.0
Spheral 4.01	43.2	48.2	51.1	51.4
Spheral 5.00	36.8	41.6	38.0	33.2
Spheral 5.01	42.4	45.8	45.3	38.5
Spheral 6.00	34.9	24.4	17.7	15.1
Spheral 6.01	39.1	29.5	19.5	17.2

Note.
[a] See Table A1 for associated maximum simulation time.

Table A3
Average Crater Diameter versus Time for FLAG Simulations

Simulation	Crater diameter (m) at 10 ms	20 ms	30 ms	40 ms	Max Sim Time	Max Simulation Time (ms)
$Y_i = 10$ Pa	6.28	7.26	7.38	7.19	9.4	51
$Y_i = 100$ Pa	6.42	6.32	7.25	6.85	14.03	110
$Y_i = 500$ Pa	6.99	8.5	9.4	9.5	10.58	80
$Y_i = 1$ kPa	7.47	7.32	8.46	8.59	14.46	130

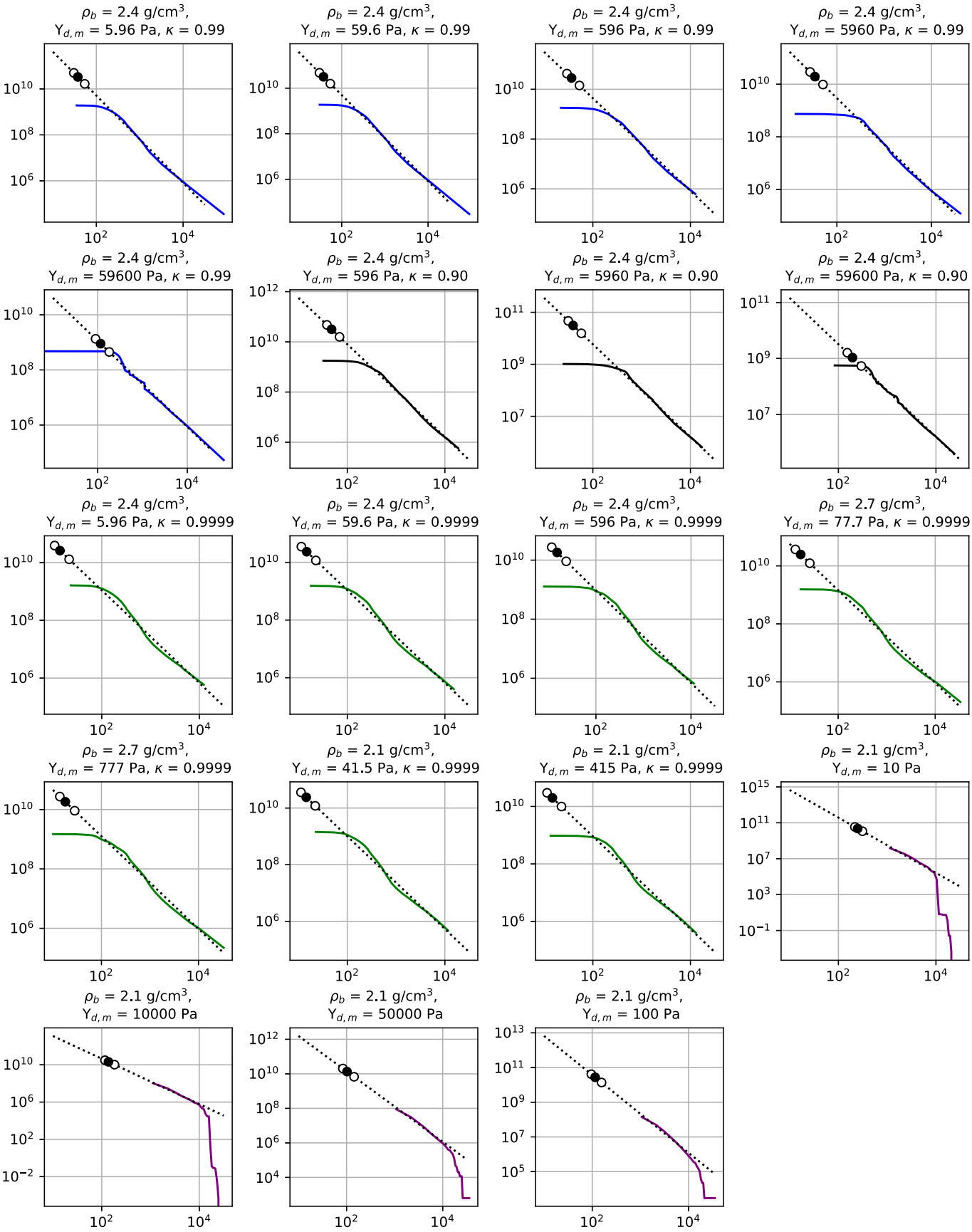

Figure A1. Cumulative ejecta mass–velocity distributions for individual simulations, from the final simulation time (see Table A1). In each panel, the x-axis is velocity in cm s^{-1}, and the y-axis is the cumulative ejecta mass in grams moving at a velocity equal to or greater than x in the antispacecraft direction. The solid colored lines are data from the simulations, and the black dotted lines are power-law fits to a portion of the cumulative ejecta curves. The solid black circle is plotted along the power-law fit at a total mass of ejecta equal to the mass of asteroid material moving in the antispacecraft direction faster than escape velocity at the maximum time reached by the simulation. The open circles show uncertainties of ±50% ejecta mass.

Table A4
Average Crater Diameter versus Time for Select CTH Simulations

10 Pa, fi = 0.6		100 Pa, fi = 0.6		500 Pa, fi = 0.6		50 kPa, fi = 0.6	
Time (ms)	Diameter (m)	Time (ms)	Diameter (m)	Time (ms)	Diameter (m)	Time (ms)	Diameter (m)
10	26	20	39.1	10	26	0	0
50	52	50	47.1	50	52	20	29.2
100	54	80	49.6	100	56	40	36.05
200	57	100	49.7	200	58	60	33.92
410	59			320	60	90	33.98

Appendix B
Simulation Parameter Details by Code and by Simulation

This appendix summarizes simulation and material model parameters used in the three main code packages for this study.

B.1. CTH

Tables B1–B3 summarize parameters used in the CTH simulations.

Table B1
Input Parameters Used in the CTH "Geo" Plasticity Model to Simulate Matrix Material

Geo Parameters (Parameter Keyword)—Matrix Material	Value
Yield, Y_i0	1 kPa
Yzero, cohesion	10 Pa, 100 Pa, 500 Pa
dydp (fi)	−0.41, −0.6, −1
Poisson	0.25
Tensile strength (pfrac)	Matched to Yzero
Porosity	58.5

Table B2
Input Parameters Used in the BDL Model to Simulate Boulders

BDL Parameter (Parameter Keyword)—Boulders	Value
Yield, Y_i0 (YM)	1 MPa
Y0, cohesion	1 kPa
CFD (fi)	1
Tensile strength (PFBDL)	0.001 MPa
Porosity	15%

Table B3
Parameters for ANEOS Dunite (Adapted from Table A1 in R. M. Canup et al. 2013)

Model Parameter	Value	Description
V1	3	Number of elements in material (Mg, Si, O)
V3	3.32 g cm^{-3}	Reference density
V4	0 eV	Reference temperature
V5	0	Reference pressure
V7	0.82	Gruneisen coefficient
V8	0.057 eV	Reference Debye temperature
V12	0.12 eV	Melting temperature

B.2. Spheral

Tables B4 and B5 summarize the properties used in Spheral simulations.

Table B4
Spheral Parameters Varied across Simulations

Sim ID	Φ_m	$Y_{i0,m}$[a] (Pa)	$Y_{d0,m}$[a] (Pa)	$Y_{d0,b}$[a] (Pa)	$f_{d,m}$	κ	Resolution (cm)	Impactor
1.00	0.404	1000	10	1000	0.6	0.99	10	Three-sphere
1.02	0.404	1000	10	1000	0.6	0.9999	10	Three-sphere
2.00	0.404	1000	100	1000	0.6	0.99	10	Three-sphere
2.02	0.404	1000	100	1000	0.6	0.9999	10	Three-sphere
2.02.1	0.585	1000	100	1000	0.6	0.9999	10	Three-sphere
2.02.2	0.223	1000	100	1000	0.6	0.9999	10	Three-sphere
4.00	0.404	1000	1000	1000	0.6	0.99	10	Three-sphere
4.00D	0.404	1000	1000	1000	0.6	0.99	10	DART spacecraft
4.01	0.404	1000	1000	1000	0.6	0.90	10	Three-sphere
4.02	0.404	1000	1000	1000	0.6	0.9999	10	Three-sphere
4.02.1	0.585	1000	1000	1000	0.6	0.9999	10	Three-sphere
4.02.2	0.223	1000	1000	1000	0.6	0.9999	10	Three-sphere
4.11[b]	0.404	1000	1000	1000	0.46	0.90	5	Three-sphere
4.12[b]	0.404	1000	1000	1000	0.46	0.90	10	Three-sphere
4.13[b]	0.404	1000	1000	1000	0.46	0.90	15	Three-sphere
5.00	0.404	10000	10000	10000	0.6	0.99	10	Three-sphere
5.01	0.404	10000	10000	10000	0.6	0.90	10	Three-sphere
6.00	0.404	100000	100000	100000	0.6	0.99	10	Three-sphere
6.01	0.404	100000	100000	100000	0.6	0.90	10	Three-sphere

Note.
[a] Y_{i0} and Y_{d0} values in this table are reported for solid material ($\varphi = 0\%$). The bulk values for Y_i and Y_d can be obtained by dividing by distension.
[b] Simulation was run with a constant sound speed in the asteroid material equivalent to solid dunite (6556 m s^{-1}) rather than reducing with porosity. The effects of sound speed on the magnitude of the resolution effect are expected to be minimal.

Table B5
Spheral Parameters Held Constant across Simulations

Parameter	Value
Minimum pressure (boulders, intact)	−1.0 MPa
Minimum pressure (matrix, intact)	Equal and opposite to $Y_{i0,m}$
Minimum pressure (boulders, damaged)	Equal and opposite to $Y_{d0,b}$
Minimum pressure (matrix, damaged)	Equal and opposite to $Y_{d0,m}$
Weibull damage for asteroid, k_{wa}	4.2×10^{25} cm^{-3}
Weibull damage for asteroid, m_{wa}	5.93
Weibull damage for impactor, k_{wi}	6.52×10^{5} cm^{-3}
Weibull damage for impactor, m_{wi}	2.63
Porous elastic compaction limit, ε_e	-1.88×10^{-4}

B.3. FLAG

Table B6 summarizes the properties used in FLAG simulations.

Table B6
Dunite Parameters for DART Impact Simulations in FLAG

FLAG Input Parameter	Value
Dunite solid density	3.32 g cm^{-3} (N. Heider & T. Kenkmann 2003)
Dunite reference bulk sound speed	6.03 m s^{-1} (N. Heider & T. Kenkmann 2003)
Dunite Gruneisen gamma	0.82 (N. Heider & T. Kenkmann 2003)
Dunite constant specific heat	0.883 J kg^{-1} K^{-1} (N. Heider & T. Kenkmann 2003)
Dunite Gruneisen S1 coefficient	0.83 (N. Heider & T. Kenkmann 2003)
Dunite boulder intact yield strength	1 MPa (R.-L. Ballouz et al. 2020)
Dunite boulder porosity	15%
Dunite boulder porous density	2.82 g cm^{-3}
Dunite matrix intact yield strength	1 kPa, 500 Pa, 100 Pa, 10 Pa
Dunite matrix porosity	22.3%
Dunite matrix porous density	2.58 g cm^{-3}
Dunite melt temperature	1698 K
Dunite Johnson−Cook parameter d1	0.05
Dunite initial shear modulus	0.5 Mbar

Appendix C
Resolution Effects

Previous studies relevant to the DART impact have been performed at a wide variety of resolutions (A. M. Stickle et al. 2020), and resolution has an effect on the calculated momentum enhancement factor. To test the effect of resolution on our exact model setup, including both the impactor composed of three spheres and the precise location of boulders used in our setup, we ran simulations with identical material parameters at multiple resolutions.

Spheral simulations examining resolution effects were run at 5, 10, and 15 cm with a bulk density of 2.4 g cm^{-3}, $Y_{d0,m}$ = 1 kPa, and $f_{d,m}$ = 0.46. These simulations used a higher sound speed in both the matrix and the boulders than the other Spheral simulations in this study (simulations 4.11–4.13 in Table A1), but the magnitude of the resolution effect is expected to be similar to the other simulations with reduced sound speed. Both β and ΔV show a strong dependence on resolution, with coarser simulations having lower values (Figure C1). This observation is consistent with previous work on homogeneous targets (A. M. Stickle et al. 2022), but the magnitude of the effect is much larger than in previous simulations. This is likely due to the large boulders placed adjacent to the impact site and directly impacted by the secondary aluminum spheres of the three-sphere impactor. These boulders produce the fastest ejecta owing to their location and their low porosity relative to the matrix. Higher-resolution impact simulations generally resolve more of the fastest ejecta than lower-resolution simulations, resulting in the larger asteroid velocity and β observed for the 5 cm simulation.

Similarly, CTH simulations examining resolution effects were run at ∼3, ∼5, ∼10, and ∼15 cm with a bulk density of 2.1 g cm^{-3} for two different cases, $Y_{d0,m}$ = 10 Pa and $f_{d,m}$ = 0.6 and $Y_{d0,m}$ = 500 Pa and $f_{d,m}$ = 1.0. Similar to the Spheral simulations, both β and ΔV show a strong dependence on resolution, with coarser simulations having lower values (Figure C2). Lower resolutions underrepresent β and ΔV owing to reduced pressure wave magnitudes; E. Pierazzo (2006) showed that a resolution of 5 cppr results in a 20% lower measured peak pressure than the same simulation with 20 cppr and reduced damage-zone extents. Further, Figure C3 plots the cumulative ejecta mass (m_e) normalized by the impactor mass (M) versus the ejecta velocity at 10, 20, and 100 ms post-impact at varying resolutions. We see that at early times (10–20 ms) the same total ejecta mass is produced at all resolutions; however, the ejecta velocity profiles are quite different, as coarse resolution grids do not capture the faster-moving ejecta material. It is likely that this trend continues out to longer time intervals (100 ms); however, our high-resolution simulations were not able to progress to these later stages. In total, we see evidence that underresolved grids underpredict β and ΔV owing to inaccuracies of the ejecta velocity profile (not the total mass).

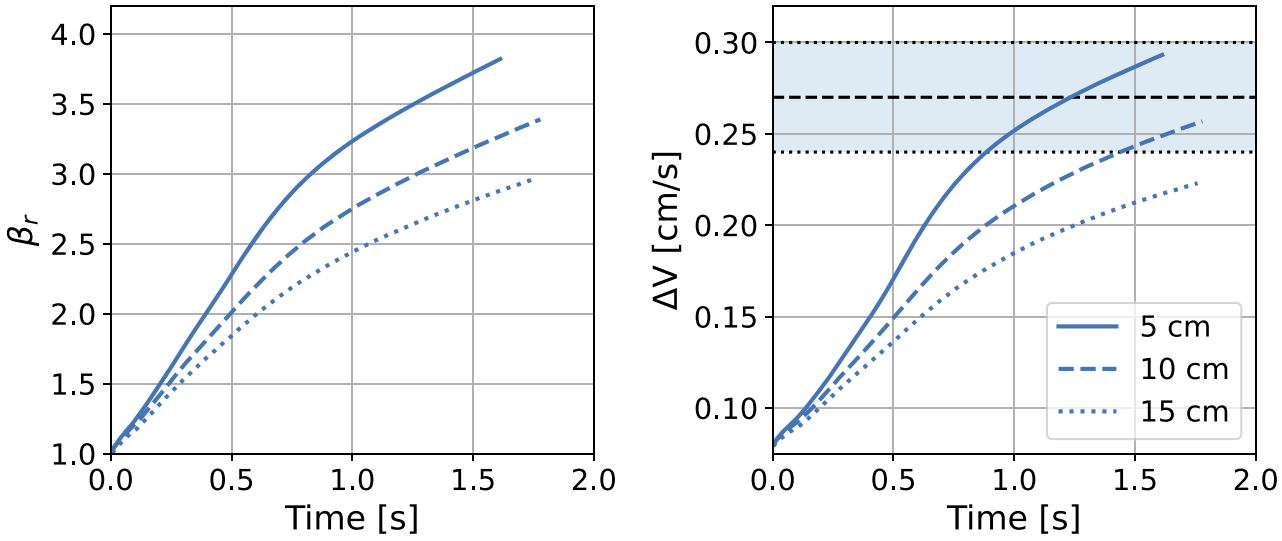

Figure C1. Spheral simulations showing the effect of simulation resolution on deflection, either β_r on the left or ΔV on the right. All material properties are kept constant between simulations. The shaded area on the right shows the observed value of ΔV based on the observed Dimorphos period change (C. A. Thomas et al. 2023) and a dynamical analysis (A. F. Cheng et al. 2023).

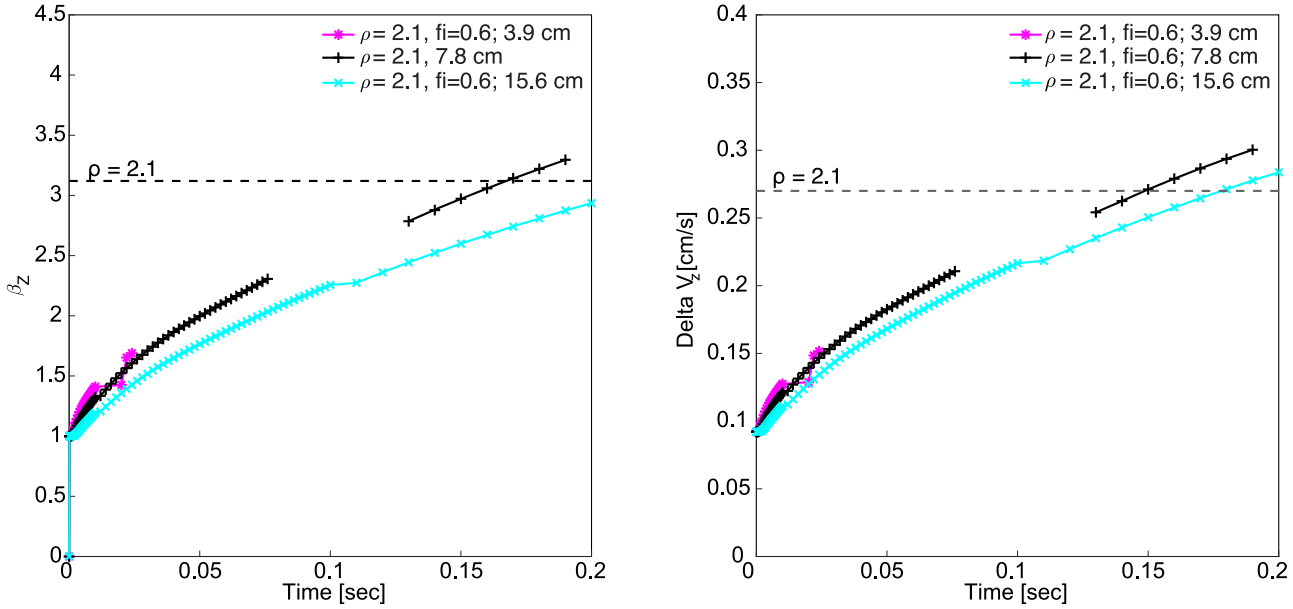

Figure C2. Resolution study for CTH simulations showing the effects of increasing resolution on β (left) and ΔV (right) for three different resolutions: 3.0, 7.8, and 15.6 cm (corresponding to 10, 4, and 2 cppr with respect to our center sphere). All material properties are kept constant between simulations. The calculated β and ΔV increase for higher-resolution simulations, suggesting that underresolved calculations provide lower limits to results.

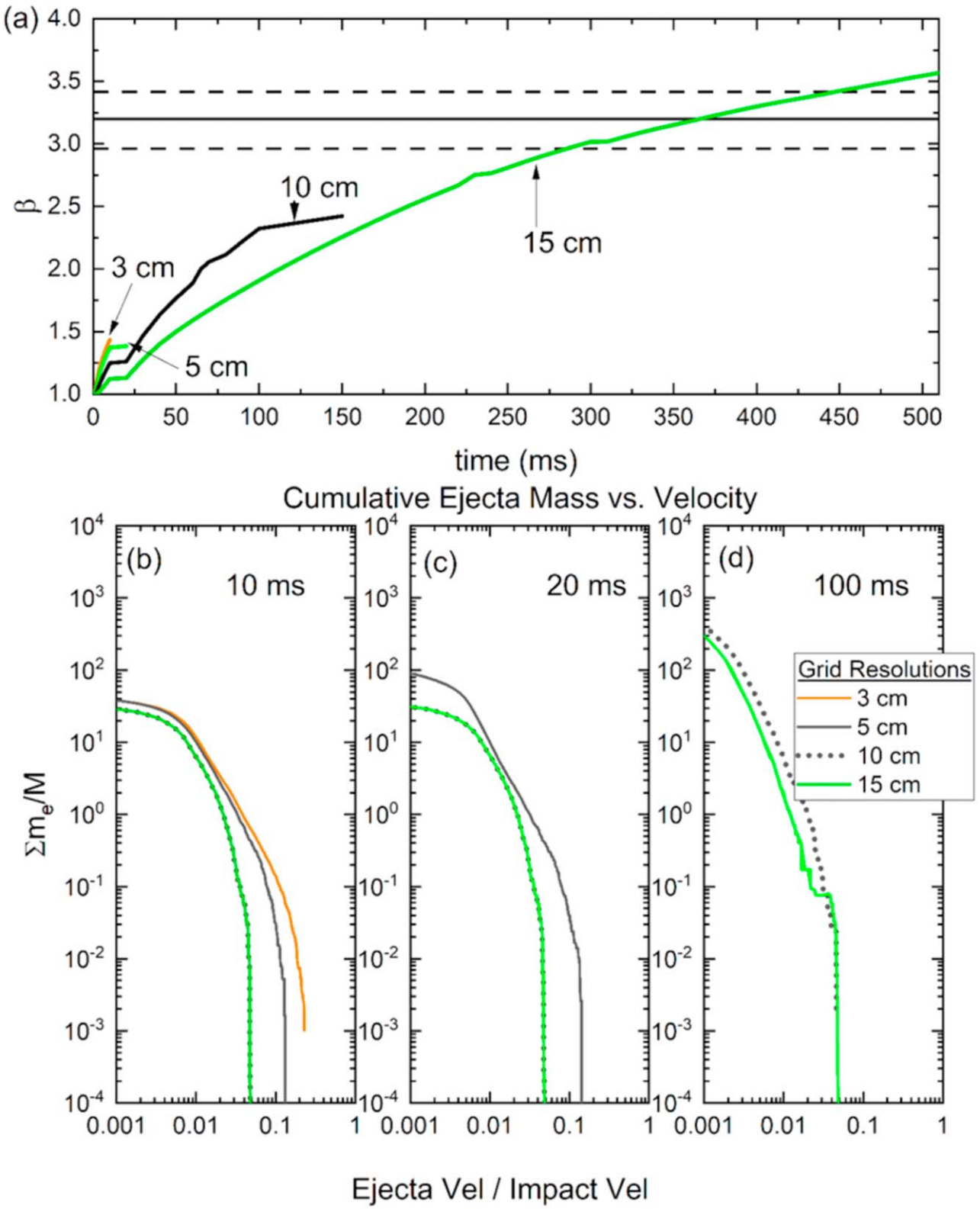

Figure C3. CTH simulations of the DART impact where $Y_{d0} = 500$ Pa, $f_{d,m} = 1$, $\rho_b = 2.1$ g cm^{-3} performed at four different grid resolutions (3, 5, 10, and 15 cm). (a) Plots of β vs. simulation time for each grid resolution, followed by the cumulative ejecta mass (m_e) normalized by the projectile mass (M) vs. the ejecta velocity normalized by the impact velocity at (*b*) 10 ms, (*c*) 20 ms, and (*d*) 100 ms post-impact.

ORCID iDs

Angela M. Stickle https://orcid.org/0000-0002-7602-9120
Kathryn M. Kumamoto https://orcid.org/0000-0002-0400-6333
Dawn M. Graninger https://orcid.org/0000-0003-1582-0581
Mallory E. DeCoster https://orcid.org/0000-0002-1139-9235
Wendy K. Caldwell https://orcid.org/0000-0001-6076-5636
Jason M. Pearl https://orcid.org/0000-0002-5340-7272
J. Michael Owen https://orcid.org/0000-0003-4796-124X
Olivier Barnouin https://orcid.org/0000-0002-3578-7750
Gareth S. Collins https://orcid.org/0000-0002-6087-6149
R. Terik Daly https://orcid.org/0000-0002-1320-2985
Isabel Herreros https://orcid.org/0000-0001-5284-8060
Jens Ormö https://orcid.org/0000-0002-5810-9442
Jessica Sunshine https://orcid.org/0000-0002-9413-8785
Carolyn M. Ernst https://orcid.org/0000-0002-9434-7886
Toshi Hirabayashi https://orcid.org/0000-0002-1821-5689
Simone Marchi https://orcid.org/0000-0003-2548-3291
Harrison Agrusa https://orcid.org/0000-0002-3544-298X
Megan Bruck Syal https://orcid.org/0000-0003-2776-9955
Nancy L. Chabot https://orcid.org/0000-0001-8628-3176
Thomas M. Davison https://orcid.org/0000-0001-8790-873X
Alice Lucchetti https://orcid.org/0000-0001-7413-3058
Robert Luther https://orcid.org/0000-0002-0745-1467
Sabina Raducan https://orcid.org/0000-0002-7478-0148
KT Ramesh https://orcid.org/0000-0003-2659-4698
Andrew S. Rivkin https://orcid.org/0000-0002-9939-9976
Alessandro Rossi https://orcid.org/0000-0001-9311-2869
Filippo Tusberti https://orcid.org/0000-0002-9290-1679
Yun Zhang https://orcid.org/0000-0003-4045-9046

References

Arakawa, M., Saiki, T., Wada, K., et al. 2020, An Artificial Impact on the Asteroid (162173) Ryugu formed a Crater in the Gravity-Dominated Regime, Sci, 368, 67
Asphaug, E. 2009, Shattered Dirt: Surface Fracture of Granular Asteorids, LPSC, 40, 1438
Bahrani, N., & Kaiser, P. K. 2020, Influence of Degree of Interlock on Confined Strength of Jointed Hard Rock Masses, JRMGE, 12, 1152
Ballouz, R.-L., Walsh, K. J., Barnouin, O. S., et al. 2020, Bennu's near-Earth Lifetime of 1.75 Million years Inferred from Craters on its Boulders, Natur, 587, 205
Barnouin, O. S., Ballouz, R. L., Marchi, S., et al. 2023, The Geology of the Didymos System, LPSC, 54, 2605
Barnouin, O. S., Daly, R. T., Cintala, M. J., & Crawford, D. A. 2019, Impacts into Coarse-Grained Spheres at Moderate Impact Velocities: Implications for Cratering on Asteroids and Planets, Icar, 325, 67
Benz, W., & Asphaug, E. 1994, Impact Simulations with Fracture. I. Method and Tests, Icar, 107, 98
Bruck Syal, M., Owen, J. M., & Miller, P. L. 2016, Deflection by Kinetic Impact: Sensitivity to Asteroid Properties, Icar, 269, 50
Burton, D. E. 1992, Connectivity Structures and Differencing Techniques for Staggered-Grid Free-Lagrange Hydrodynamics UCRL-JC-110555, Lawrence Livermore National Laboratory, https://www.osti.gov/biblio/7047398
Burton, D. E. 1994a, Consistent Finite-Volume Discretization of Hydrodynamic Conservation Laws for Unstructured Grids UCRL-JC-118788, Lawrence Livermore National Laboratory, https://www.osti.gov/biblio/71618
Burton, D. E. 1994b, Multidimensional Discretization of Conservation Laws for Unstructured Polyhedral Grids UCRL-JC-118306, Lawrence Livermore National Laboratory, https://www.osti.gov/biblio/35336
Burton, D. E., Morgan, N. R., Charest, M. R. J., Kenamond, M. A., & Fung, J. 2018, Compatible, Energy Conserving, Bounds Preserving Remap of Hydrodynamic Fields for an Extended ALE Scheme, JCoPh, 355, 492
Caldwell, W. K. 2019, Differential equation Models for Understanding Phenomena beyond Experimental Capabilities, PhD thesis, Univ. Arizona
Caldwell, W. K., Euser, B., Plesko, C. S., et al. 2021, Benchmarking Numerical Methods for Impact and Cratering Applications, ApSci, 11, 2504
Caldwell, W. K., Hunter, A., Plesko, C. S., & Wirkus, S. 2018, Verification and Validation of the FLAG Hydrocode for Impact Cratering Simulations, Journal of Verification, Validation and Uncertainty Quantification, 3, 031004
Canup, R. M., Barr, A. C., & Crawford, D. A. 2013, Lunar-Forming Impacts: High-Resolution SPH and AMR-CTH Simulations, Icar, 222, 200
Carrier, W. D., Olhoeft, G. R., & Mendell, W. 1991, Physical Properties of the Lunar Surface, in Lunar Sourcebook, ed. G. H. Heiken, D. T. Vaniman, & B. M. French (New York: Cambridge Univ. Press), 475
Cheng, A. F., Agrusa, H. F., Barbee, B. W., et al. 2023, Momentum Transfer from the DART Mission Kinetic Impact on Asteroid Dimorphos, Natur, 616, 457
Cheng, A. F., Raducan, S. D., Fahnestock, E. G., et al. 2022, Model of Double Asteroid Redirection Test Impact Ejecta Plume Observations, PSJ, 3, 131
Cheng, A. F., Rivkin, A. S., Michel, P., et al. 2018, AIDA DART Asteroid Deflection Test: Planetary Defense and Science Objectives, P&SS, 157, 104
Collins, G. S., Melosh, H. J., & Ivanov, B. A. 2004, Modeling Damage and Deformation in Impact Simulations, M&PS, 39, 217
Collins, G. S., Melosh, H. J., & Wünnemann, K. 2011, Improvements to the ε-α Porous Compaction Model for Simulating Impacts into High-Porosity Solar System Objects, IJIE, 38, 434
Crawford, D. A. 1999, Adaptive Mesh Refinement in CTH SAND99-1118C, Sandia National Laboratories (SNL), https://www.osti.gov/biblio/7235
Daly, R. T., Ernst, C. M., Barnouin, O. S., et al. 2023, Successful Kinetic Impact into an Asteroid for Planetary Defence, Natur, 616, 443
Daly, R. T., Ernst, C. M., Barnouin, O. S., et al. 2024, An Updated Shape Model of Dimorphos from DART Data, PSJ, 5, 24
Daly, T., Barnouin, O., Ernst, C., et al. 2023, Derived Data Products for DART Shapemodel: didymos_model_v003, NASA Planetary Data System, doi:10.26007/bm57-x327
DeCoster, M. E., Luther, R., Collins, G. S., et al. 2024, The Relative Effects of Surface and Subsurface Morphology on the Deflection Efficiency of Kinetic Impactors: Implications for the DART Mission, PSJ, 5, 21
DeCoster, M. E., Rainey, E. S. G., Rosch, T. W., & Stickle, A. M. 2022, Statistical Significance of Mission Parameters on the Deflection Efficiency of Kinetic Impacts: Applications for the Next-generation Kinetic Impactor, PSJ, 3, 186
Deshapriya, J. D. P., Hasselmann, P. H., Gai, I., et al. 2023, Characterization of the DART Impact Ejecta Plume on Dimorphos from LICIACube Observations, PSJ, 4, 231
Dotto, E., Della Corte, V., Amoroso, M., et al. 2021, LICIACube - The Light Italian Cubesat for Imaging of Asteroids in support of the NASA DART Mission towards Asteroid (65803) Didymos, P&SS, 199, 105185
Dotto, E., Deshapriya, J. D. P., Gai, I., et al. 2024, The Dimorphos Ejecta Plume Properties Revealed by LICIACube, Natur, 627, 505
Elbeshausen, D., Wünnemann, K., & Collins, G. S. 2009, Scaling of Oblique Impacts in Frictional Targets: Implications for Crater Size and Formation Mechanisms, Icar, 204, 716
Fang, Z., Patterson, B. R., & Turner, M. E. 1993, Modeling Particle Size Distributions by the Weibull Distribution Function, Materials Characterization, 31, 177
Farnham, T. L., Hirabayashi, M., Deshapriya, J. D. P., et al. 2023, 3D Characterization of the Ejecta Produced by the DART Impact in Asteroids, Comets, Meteors Conf. 2851, 2127
Ferrari, F., Panicucci, P., Merisio, G., et al. 2024, Morphology of Ejecta Features from the DART Impact on Dimorphos and their Implications, NatAs, submitted
Fletcher, Z. J., Ryan, K. J., Maas, B. J., et al. 2018, Design of the Didymos Reconnaissance and Asteroid Camera for OpNav (DRACO) on the Double Asteroid Redirection test (DART), Proc. SPIE, 10698, 106981X
Flynn, G. J., Consolmagno, G. J., Brown, P., & Macke, R. J. 2018, Physical Properties of the Stone Meteorites: Implications for the Properties of their Parent Bodies, ChEG, 78, 269
Grady, D. E., & Kipp, M. E. 1980, Continuum Modelling of Explosive Fracture in Oil Shale, IJRMA, 17, 147
Graykowski, A., Lambert, R. A., Marchis, F., et al. 2023, Light Curves and Colours of the Ejecta from Dimorphos after the DART Impact, Natur, 616, 461

Heider, N., & Kenkmann, T. 2003, Numerical Simulation of Temperature Effects at Fissures Due to Shock Loading, M&PS, 38, 1451
Herrmann, W. 1969, Constitutive Equation for the Dynamic Compaction of Ductile Porous Materials, JAP, 40, 2490
Hill, J. L. 2017, Manual for FLAG version 3.6.0. LA-CP-17-20057, Los Alamos National Laboratory
Hirabayashi, M., Raducan, S. D., Sunshine, J. M., et al. 2024, Kinetic Deflection Change Due to Target Global Curvature as Revealed by NASA/DARTNatCo, Natur, submitted
Holsapple, K. A., & Housen, K. R. 2007, A Crater and Its Ejecta: An Interpretation of Deep Impact, Icar, 191, 586
Holsapple, K. A., & Housen, K. R. 2012, Momentum Transfer in Asteroid Impacts. I. Theory and Scaling, Icar, 221, 875
Housen, K. R., Holsapple, K. A., & Voss, M. E. 1999, Compaction as the Origin of the Unusual Craters on the Asteroid Mathilde, Natur, 402, 155
Jewitt, D., Kim, Y., Li, J., & Mutchler, M. 2023, The Dimorphos Boulder Swarm, ApJL, 952, L12
Johnson, G. R., & Cook, W. H. 1985, Fracture Characteristics of Three Metals Subjected to Various Strains, Strain Rates, Temperatures and Pressures, EnFM, 21, 31
Jutzi, M., Raducan, S. D., Zhang, Y., Michel, P., & Arakawa, M. 2022, Constraining Surface Properties of Asteroid (162173) Ryugu from Numerical Simulations of Hayabusa2 Mission Impact Experiment, NatCo, 13, 7134
Kadono, T., Suetsugu, R., Arakawa, D., et al. 2019, Pattern of Impact-Induced Ejecta from Granular Targets with Large Inclusions, ApJL, 880, L30
Kareta, T., Thomas, C., Li, J-Y., et al. 2023, Ejecta Evolution Following a Planned Impact Into an Asteroid: The First Five Weeks, ApJL, 959, L12
Kim, Y., & Jewitt, D. 2023, A Single Ejection Model of the DART Dimorphos Debris Trail, ApJL, 956, L26
Krantz, R. W. 1991, Measurements of Friction Coefficients and Cohesion for Faulting and Fault Reactivation in Laboratory Models Using Sand and Sand Mixtures, Tectp, 188, 203
Kumamoto, K. M., Michael Owen, J., Syal, M. B., et al. 2022, Predicting Asteroid Material Properties from a DART-like Kinetic Impact, PSJ, 3, 237
Lee, P. 1996, Dust Levitation on Asteroids, Icar, 124, 181
Li, J. Y., Hirabayashi, M., Farnham, T. L., et al. 2023, Ejecta from the DART-Produced Active Asteroid Dimorphos, Natur, 616, 452
Luther, R., Raducan, S. D., Burger, C., et al. 2022, Momentum Enhancement during Kinetic Impacts in the Low-intermediate-strength Regime: Benchmarking and Validation of Impact Shock Physics Codes, PSJ, 3, 227
Marchi, S., Chapman, C. R., Barnouin, O. S., Richardson, J. E., & Vincent, J-B. 2015, Cratering on Asteroids, in Asteroids IV, ed. P. Michel, F. E. DeMeo, & W. F. Bottke (Tucson, AZ: Univ. Arizona Press)
Marshall, J. R., Sauke, T. B., & Cuzzi, J. N. 2005, Microgravity Studies of Aggregation in Particulate Clouds, GeoRL, 32, L11202
McGlaun, J. M., Thompson, S. L., & Elrick, M. G. 1990, CTH: A Three-Dimensional Shock Wave Physics Code, IJIE, 10, 351
McKay, D. S., Heiken, G., Basu, A., et al. 1991, The Lunar Regolith, in Lunar Sourcebook: A Users Guide to the Moon, ed. G. H. Heiken, D. T. Vaniman, & B. M. French (Cambridge: Cambridge Univ. Press), 285
Melosh, H. J. 2007, A Hydrocode Equation of State for SiO2, M&PS, 42, 2079
Michel, P., Küppers, M., Bagatin, A. C., et al. 2022, The ESA Hera Mission: Detailed Characterization of the DART Impact Outcome and of the Binary Asteroid (65803) Didymos, PSJ, 3, 160
Moreno, F. C., Bagatin, A., Tancredi, G., Li, J.-Y., Rossi, A., Ferrari, F., et al. 2023, Characterization of the Ejecta from the NASA/DART Impact on Dimorphos: Observations and Monte Carlo Models, PSJ, 4, 138
Murchie, S. L., Thomas, P. C., Rivkin, A. S., & Chabot, N. L. 2015, Phobos and Deimos, in Asteroids IV, ed. P. Michel, F. E. DeMeo, & W. F. Bottke (Tucson, AZ: Univ. Arizona Press), 451
Naidu, S. P., Chesley, S. R., Moskovitz, N., et al. 2024, Orbital and Physical Characterization of Asteroid Dimorphos Following the DART Impact, PSJ, 5, 74
Ormö, J., Raducan, S. D., Jutzi, M., et al. 2022, Boulder Exhumation and Segregation by Impacts on Rubble-Pile Asteroids, E&PSL, 594, 117713
Owen, J. M. 2010, ASPH Modeling of Material Damage and Failure, 5th Int. SPHERIC SPH Workshop LLNL-PROC-430616, Lawrence Livermore National Lab (LLNL), https://www.osti.gov/biblio/1009644
Owen, J. M., DeCoster, M. E., Graninger, D. M., & Raducan, S. D. 2022, Spacecraft Geometry Effects on Kinetic Impactor Missions, PSJ, 3, 218
Owen, J. M., Villumsen, J. V., Shapiro, P. R., & Martel, H. 1998, Adaptive Smoothed Particle Hydrodynamics: Methodology II, ApJS, 116, 155
Pacheco-Vázquez, F. 2019, Ray Systems and Craters Generated by the Impact of Nonspherical Projectiles, PhRvL, 122, 164501
Pajola, M., Tusberti, F., Lucchetti, A., et al. 2024, Evidence for Multi-Fragmentation and Mass Shedding of Boulders on Rubble-Pile Binary Asteroid System (65803) Didymos, NatCo, 15, 6205
Pearl, J. M., Raskin, C. D., & Michael Owen, J. 2022, FSISPH: An SPH Formulation for Impacts between Dissimilar Materials, JCoPh, 469, 111533
Pierazzo, E. 2006, Numerical Modeling of Impact Cratering, ESA Spec. Publ., SP, 612, 115, https://sci.esa.int/documents/33321/35974/1567255427042-ESLAB40-Proc_298069-Pierazzo.pdf
Pravec, P., Meyer, A. J., Scheirich, P., et al. 2024, Rotational Lightcurves of Dimorphos and Constraints on its Post-DART Impact Spin State, Icar, 418, 116138
Quintana, S. N., Crawford, D. A., & Schultz, P. H. 2015, Analysis of Impact Melt and Vapor Production in CTH for Planetary Applications, PrEng, 103, 499
Raducan, S. D., Davison, T. M., & Collins, G. S. 2022a, Ejecta Distribution and Momentum Transfer from Oblique Impacts on Asteroid Surfaces, Icar, 374, 114793
Raducan, S. D., Davison, T. M., Luther, R., & Collins, G. S. 2019, The Role of Asteroid Strength, Porosity and Internal Friction in Impact Momentum Transfer, Icar, 329, 282
Raducan, S. D., & Jutzi, M. 2022, Global-scale Reshaping and Resurfacing of Asteroids by Small-Scale Impacts, with Applications to the DART and Hera Missions, PSJ, 3, 128
Raducan, S. D., Jutzi, M., Cheng, A. F., et al. 2024, Physical Properties of Asteroid Dimorphos as Derived from the DART Impact, NatAs, 8, 445
Raducan, S. D., Jutzi, M., Davison, T. M., et al. 2022b, Influence of the Projectile Geometry on the Momentum Transfer from a Kinetic Impactor and Implications for the DART Mission, IJIE, 162, 104147
Rainey, E. S. G., Stickle, A. M., Cheng, A. F., et al. 2020, Impact Modeling for the Double Asteroid Redirection Test (DART) Mission, IJIE, 142, 103528
Richardson, D. C., Agrusa, H. F., Barbee, B., et al. 2024, The Dynamical State of the Didymos System Before and After the DART Impact, PSJ, 5, 182
Rivkin, A. S., Chabot, N. L., Stickle, A. M., et al. 2021, The Double Asteroid Redirection Test (DART): Planetary Defense Investigations and Requirements, PSJ, 2, 173
Roth, N. X., Milam, S. N., Remijan, A. J., et al. 2023, ALMA Observations of the DART Impact: Characterizing the Ejecta at Submillimeter Wavelengths, PSJ, 4, 206
Rozitis, B., Ryan, A. J., Emery, J. P., et al. 2022, High-Resolution Thermophysical Analysis of the OSIRIS-REx Sample Site and Three other Regions of Interest on Bennu, JGRE, 127, e07153
Sabuwala, T., Butcher, C., Gioia, G., & Chakraborty, P. 2018, Ray Systems in Granular Cratering, PhRvL, 120, 264501
Scheeres, D. J. 2005, Solar Radiation Pressure and Transient Flows on Asteroid Surfaces, LPSC, 36, 1919
Scheeres, D. J., Hartzell, C. M., Sánchez, P., & Swift, M. 2010, Scaling Forces to Asteroid Surfaces: The role of Cohesion, Icar, 210, 968
Schultz, P. H., & Crawford, D. A. 2016, Origin and Implications of Non-radial Imbrium Sculpture on the Moon, Natur, 535, 391
Schultz, P. H., Eberhardy, C. A., Ernst, C. M., et al. 2007, The Deep Impact Oblique Impact Cratering Experiment, Icar, 191, 84
Schultz, P. H., & Gault, D. E. 1985, Clustered Impacts: Experiments and Implications, JGR, 90, 3701
Senft, L. E., & Stewart, S. T. 2009, Dynamic Fault Weakening and the Formation of Large Impact Craters, E&PSL, 287, 471
Schwartz, S. R., Yu, Y., Michel, P., & Jutzi, M. 2016, Small–body Deflection Techniques using Spacecraft: Techniques in Simulating the Fate of Ejecta, AdSpR, 57, 1832
Shuvalov, V. 2012, A Mechanism for the Production of Crater Rays, M&PS, 47, 262
Statler, T. S., Raducan, S. D., Barnouin, O. S., et al. 2022, After DART: Using the First Full-scale Test of a Kinetic Impactor to Inform a Future Planetary Defense Mission, PSJ, 3, 244
Stewart, S. T., Davies, E. J., Duncan, M. S., et al. 2019, Equation of State Model Forsterite-ANEOS-SLVTv1.0G1: Documentation and Comparisons, v1.0.0, Zenodo, doi:10.5281/zenodo.3478631
Stickle, A. M., Atchison, J. A., Barnouin, O. S., et al. 2015, Modeling Momentum Transfer from Kinetic Impacts: Implications for Redirecting Asteroids, PrEng, 103, 577
Stickle, A. M., Bruck Syal, M., Cheng, A. F., et al. 2020, Benchmarking Impact Hydrocodes in the Strength Regime: Implications for Modeling Deflection by a Kinetic Impactor, Icar, 338, 113446
Stickle, A. M., Burger, C., Caldwell, W. K., et al. 2022, Effects of Impact and Target Parameters on the Results of a Kinetic Impactor: Predictions for the Double Asteroid Redirection Test (DART) Mission, PSJ, 3, 248

Stickle, A. M., Rainey, E. S. G., Syal, M. B., et al. 2017, Modeling Impact Outcomes for the Double Asteroid Redirection Test (DART) mission, PrEng, 204, 116
Tatsumi, E., & Sugita, S. 2018, Cratering Efficiency on Coarse-Grain Targets: Implications for the Dynamical Evolution of Asteroid 25143 Itokawa, Icar, 300, 227
Thomas, C. A., Naidu, S. P., Scheirich, P., et al. 2023, Orbital Period Change of Dimorphos Due to the DART Kinetic Impact, Natur, 616, 448
Thompson, S. L. 1990, ANEOS Analytic Equations of State for Shock Physics Codes Input Manual SAND-89-2951, Sandia National Labs
Thompson, S. L., & Lauson, H. S. 1972, Improvements in the Chart D· Radiation-Hydrodynamic CODE III: Revised Analytic Equations of State SC-RR-710714, Sandia National Laboratories
Thompson, S. L., Lauson, H. S., Melosh, H. J., Collins, G. S., & Stewart, S. T. 2019, M-ANEOS: A Semi-Analytical equation of State Code, v1, Zenodo, doi:10.5281/zenodo.3525030
Tillotson, J. H. 1962, Metallic equations of state for hypervelocity impact GA-3216, General Atomic Division, General Dynamics, Air Force Weapons Lab
Trucano, T. G., & McGlaun, J. M. 1990, Hypervelocity Impact Calculations Using CTH: Case Studies, IJIE, 10, 601
Turtle, E. P., Pierazzo, E., Collins, G. S., et al. 2005, Impact Structures: What Does Crater Diameter Mean, in Large Meteorite Impacts III, ed. T. Kenkmann, F. Hörz, & A. Deutsch, Vol. 384 (Boulder, CO: Geological Society of America), 1
Voropaev, S. A., Kocherov, A. V., Lorenz, C. A., et al. 2017, Features in Constructing a Certificate of Strength of Extraterrestrial Material by the Example of the Chelyabinsk Meteorite, DokPh, 62, 486
Walker, J. D., & Chocron, S. 2011, Momentum Enhancement in Hypervelocity Impact, IJIE, 38, A1
Wünnemann, K., Collins, G. S., & Melosh, H. J. 2006, A Strain-Based Porosity Model for Use in Hydrocode Simulations of Impacts and Implications for Transient Crater Growth in Porous Targets, Icar, 180, 514